JOURNAL OF GEOPHYSICAL RESEARCH, VOL. 113, D02203, doi:10.1029/2007JD008434, 2008

Solar radiation budget and radiative forcing due to aerosols and clouds

Dohyeong Kim[1,2] and V. Ramanathan[1]

Received 18 January 2007; revised 23 July 2007; accepted 12 September 2007; published 19 January 2008.

[1] This study integrates global data sets for aerosols, cloud physical properties, and shortwave radiation fluxes with a Monte Carlo Aerosol-Cloud-Radiation (MACR) model to estimate both the surface and the top-of-atmosphere (TOA) solar radiation budget as well as atmospheric column solar absorption. The study also quantifies the radiative forcing of aerosols and that of clouds. The observational input to MACR includes data from the Multiangle Imaging Spectroradiometer (MISR) for aerosol optical depths, single scattering albedos, and asymmetry factors; satellite retrieved column water vapor amount; the Total Ozone Mapping Spectrometer (TOMS) total ozone amount; and cloud fraction and cloud optical depth from the Cloud and Earth's Radiant Energy System (CERES) cloud data. The present radiation budget estimates account for the diurnal variation in cloud properties. The model was validated against instantaneous, daily and monthly solar fluxes from the ground-based Baseline Surface Radiation Network (BSRN) network, the Global Energy Balance Archive (GEBA) surface solar flux data, and CERES TOA measurements. The agreement between simulated and observed values are within experimental errors, for all of the cases considered here: instantaneous fluxes and monthly mean fluxes at stations around the world and TOA fluxes and cloud forcing for global annual mean and zonal mean fluxes; in addition the estimated aerosol forcing at TOA also agrees with other observationally derived estimates. Overall, such agreements suggest that global data sets of aerosols and cloud parameters released by recent satellite experiments (MISR, MODIS and CERES) meet the required accuracy to use them as input to simulate the radiative fluxes within instrumental errors. Last, the atmospheric solar absorption derived in this study should be treated as an improved estimate when compared with earlier published studies. The main source of improvement in the present estimate is the use of global distribution of observed parameters for model input such as aerosols and clouds. The agreement between simulated and observed solar fluxes at the surface supports our conclusion that the present estimate is an improvement over previous studies. MACR with the global input data was used to simulate the global and regional solar radiation budget, aerosol radiative forcing and cloud radiative forcing for a 3-year period from 2000 to 2002. We estimate the planetary albedo for a 3-year average to be 28.9 ± 1.2% to be compared with CERES estimate of 28.6% and ERBE's estimate of 29.6%. Without clouds (including aerosols) the planetary albedo is only 15.0 ± 0.6%. The global mean TOA shortwave cloud forcing is -47.5 ± 4 W m^{-2}, comparing well with the CERES and ERBE estimates of -46.5 and -48 W m^{-2}, respectively. The clear-sky atmospheric absorption is 72 ± 3 W m^{-2}, and the surface absorption is 218 ± 4 W m^{-2}. Clouds in all-sky conditions enhance atmospheric absorption from 72 ± 3 W m^{-2} to 79 ± 5 W m^{-2} and decrease surface solar absorption from 218 ± 4 W m^{-2} to 164 ± 6 W m^{-2}. The present estimate of 79 W m^{-2} for all-sky solar absorption is much larger than the Intergovernmental Panel on Climate Change (2001) values of about 67 W m^{-2}. Most of the increased atmospheric solar absorption is due to improved treatment of aerosol absorption (backed by surface based aerosol network and chemical transport models) and water vapor spectroscopic data. The global mean clear-sky aerosol (both natural and anthropogenic) radiative forcing at the

[1]Center for Clouds, Chemistry and Climate, Scripps Institution of Oceanography, La Jolla, California, USA.
[2]Now at Korea Meteorological Administration, Seoul, South Korea.

0148-0227/08/2007JD008434$09.00

TOA and the surface are -6.0 ± 1 W m^{-2} and -11.0 ± 2 W m^{-2}, respectively. In the presence of clouds the aerosol radiative forcing is -3.0 ± 1 W m^{-2} (at TOA) and -7.0 ± 2 W m^{-2} (at the surface). The study also documents the significant regional variations in the solar radiation budget and radiative forcing of aerosols and clouds.

Citation: Kim, D., and V. Ramanathan (2008), Solar radiation budget and radiative forcing due to aerosols and clouds, *J. Geophys. Res.*, *113*, D02203, doi:10.1029/2007JD008434.

1. Introduction

[2] Large reductions in solar radiation at the surface over multidecadal timescales have been reported by numerous studies [e.g., *Stanhill and Cohen*, 2001; *Liepert*, 2002; *Ramanathan et al.*, 2005]. These decadal-scale reductions are based upon widespread observations of surface solar radiation and range from -2 W m^{-2} to -5 W m^{-2} per decade. Using surface measured and satellite retrieved data, *Wild et al.* [2005] and *Pinker et al.* [2005] reported that the surface solar radiation decreased from 1960 to 1990, but then increased after that period. The sources of these changes are attributed to changes in aerosols, clouds or both. Field studies have revealed that aerosols by themselves can lead to changes as large as those observed. For example, observations from the Indian Ocean Experiment [*Ramanathan et al.*, 2001a] documented with chemical, microphysical and radiation data that absorbing aerosols from human activities can spread over vast areas of the Indian Ocean because of long-range transport and reduce seasonal mean solar radiation absorbed over the entire northern Indian Ocean by as much as 14 W m^{-2} (about 7% of surface downwelling solar radiation over the entire northern Indian Ocean). Numerous field studies around the world have confirmed these findings [e.g., *Conant*, 2000; *Kim et al.*, 2005; *Russell et al.*, 1999; *Ramanathan and Ramana*, 2005; *Yu et al.*, 2006]. Aerosol-cloud interactions can contribute to additional large-scale decrease in the surface solar radiation [e.g., *Kaufman et al.*, 2005a]. Moreover, the presence of clouds can significantly change the radiative impact of aerosols, especially when absorbing aerosols are located above the clouds [e.g., *Liao and Seinfeld*, 1998b; *Haywood and Ramaswamy*, 1998; *Myhre et al.*, 2003]. These theoretical studies are consistent with large dimming of the sort revealed in the *Stanhill and Cohen* [2001] and *Liepert* [2002] studies. Therefore understanding the role of aerosol/cloud in solar radiation is crucial to understanding the observed changes in solar radiation. The reduction in the surface solar radiation can profoundly influence evaporation, surface temperature, and the hydrological cycle [e.g., *Ramanathan et al.*, 2001b; *Roderick and Farquhar*, 2002; *Ohmura and Wild*, 2002; *Ramanathan et al.*, 2005].

[3] Apart from the importance of changes in solar radiation, significant uncertainty persists in our understanding of atmospheric solar absorption in clear and all skies [*Arking*, 1996; *Gilgen and Ohmura*, 1999; *Ramanathan and Vogelmann*, 1997]. Models in the past typically underestimate solar absorption by magnitudes ranging from 10 to 25 W m^{-2} (diurnal-monthly to annual mean values; see summary given by *Ramanathan and Vogelmann* [1997]). Clearly there is a great need to refine and understand the solar radiation budget of the planet.

[4] In spite of efforts to accurately incorporate the role of aerosol/clouds in global models, there are large discrepancies between various model results [*Halthore et al.*, 2005; *Collins et al.*, 2002] as well as between models and observations [e.g., *Ramanathan and Vogelmann*, 1997; *Li et al.*, 1997]. We believe that these inconsistencies stem from the many inherent assumptions involved in simulating the aerosol/cloud effect on climate. The large uncertainties come from assumptions concerning the physical and chemical properties of aerosols as well as aerosol-cloud-radiation interactions. In order to reduce the uncertainties in global studies, an integrated approach using reliable multiple data sources, e.g., ground-based, satellite, and model retrieved data [e.g., *Boucher and Tanre*, 2000; *Chou et al.*, 2002; *Christopher and Zhang*, 2002; *Yu et al.*, 2004, 2006] and accurate radiative transfer models are required. For example, *Chou et al.* [2002] used the aerosol properties from the Sea-viewing Wide Field-of-view Sensor (SeaWiFS). *Yu et al.* [2004] combined MODIS data and the Georgia Tech/Goddard Global Ozone Chemistry Aerosol Radiation and Transport (GOCART) which was then evaluated with measurements from the Aerosol Robotic Network (AERONET). *Boucher and Tanre* [2000] used the Polarization and Directionality of the Earth's Reflectances (POLDER) satellite retrievals for aerosol properties. *Zhang et al.* [2005a, 2005b] developed an independent method by using the Clouds and the Earth's Radiant Energy System (CERES) satellite derived fluxes at the TOA and correlating these with satellite-retrieved AODs to derive aerosol radiative forcing similar to the method adopted by *Satheesh and Ramanathan* [2000].

[5] Our main objectives are to accurately simulate the measured solar radiation at both the surface and the top of the atmosphere (TOA), and to quantify the role of aerosols and clouds in the global solar radiation field. Contrasting with previous work, this study takes an alternate approach and relies mainly on observations from satellites and ground-based measurements for the model input parameters such as clouds, aerosols, water vapor, surface albedo and ozone. The main advantage of this method is that the radiation calculation is not subject to deficiencies in the GCM simulations because aforementioned parameters are constrained by observations. Furthermore, we validate our model and the input by comparing the simulated radiation fluxes at the surface and at TOA with radiometric observations. Thus this study makes an optimum use of available observations and provides an observationally constrained estimate for radiation budget and atmospheric solar absorption. For aerosol parameters (aerosol optical depth (AOD), single scattering albedo (SSA) and asymmetry factor), the quality assured level 2.0 data from the AERONET was used [e.g., *Dubovik et al.*, 2000, 2002; *Holben et al.*, 2001]. The Multiangle Imaging Spectroradiometer (MISR) AODs [e.g., *Diner et al.*, 1998; *Kahn et al.*, 2001, 2005] and The

Moderate resolution Imaging Spectroradiometer (MODIS) AODs [e.g., *Kaufman et al.*, 1997; *Tanre et al.*, 1997; *Remer et al.*, 2005] are used for global distribution of AODs. An assimilated MISR + AERONET _AOD data set was also tested in MACR and the resulting global radiation budget estimates were compared with the results from MISR and MODIS AODs. The details of the assimilation procedure are described by *Chung et al.* [2005]. Both the CERES clouds and International Satellite Cloud Climatology Project (ISCCP)-D2 monthly mean cloud data [*Rossow and Schiffer*, 1999] are used for all-sky flux calculation. The use of multiple cloud and aerosol data sets enabled us to quantify the uncertainties introduced by uncertainties in input data sets.

[6] The present study uses the Monte Carlo Aerosol-Cloud-Radiation (MACR) model developed by our group [*Podgorny et al.*, 2000; *Podgorny and Ramanathan*, 2001; *Vogelmann et al.*, 2001; *Chung et al.*, 2005]. MACR was run at instantaneous, daily and monthly resolutions for accurate comparison and validation with ground-based and satellite measurements. BSRN station data, which include AERONET AOD and aerosol single scattering albedo (SSA) measurements are used for instantaneous (i.e., various solar zenith angles) flux comparison for model validation under clear-sky conditions. MISR AODs for comparison with the surface based daily BSRN and monthly GEBA measurements are used to quantify the error in MACR estimates of daily and monthly average fluxes. CERES retrievals of TOA albedos over the stations provide a means to quantify the errors in the MACR predictions of TOA albedos. Such comparisons and validations are of course limited by uncertainties in the measurements themselves. We use available literature values for the measurement uncertainties.

[7] Data from multiple platforms, including MISR and MODIS for AODs and CERES and ISCCP for clouds were used to obtain the global aerosol and cloud parameters, which were then used to estimate the global radiation budget. The source of data used for input to the radiation model and validation data at the surface and TOA are summarized in section 2. The radiative transfer model used for calculating the solar radiative fluxes is described in section 3. Section 4 compares the calculated fluxes with ground-based measurements. Section 5 presents the results of model calculated global solar fluxes, and aerosol/cloud radiative forcing at the TOA, in the atmosphere, and at the surface. Comparisons of the model calculated fluxes and radiative forcing at the TOA with satellite retrievals are given in section 5, followed by conclusions in the last section.

2. Data

[8] For the MACR evaluation of comparison, instantaneous, daily and monthly mean values at a given validation site were used. When model inputs were unavailable at a given site, we used daily mean values on a 1° by 1° grid. Climatological monthly mean values on a spatial T42 grid (approximately 2.8° by 2.8°) were used for the estimation of global solar radiation budget. For this, the data with different resolution were interpolated onto the T42 resolution by averaging the data over each T42 grid.

2.1. MACR Input Data

2.1.1. AERONET

[9] AERONET is a worldwide network of ground-based, automated Sun photometers deployed by the NASA Goddard Space Flight Center since 1993 [e.g., *Holben et al.*, 1998, 2001]. The AERONET provides data on spectral aerosol properties and precipitable water. AERONET measurement uncertainties are well understood [e.g., *Dubovik et al.*, 2000] and the data widely used as a standard for satellite aerosol retrieval validation. Thus the aerosol parameters and uncertainties are suitable for model validation. The quality assured level 2 data product for AOD, SSA and asymmetry factors of 0.44, 0.675, 0.87, and 1.02 μm were used. In some instance, SSA data were not available even though AOD and asymmetry factor exist. In such cases, we used level 1.5 version (i.e., real time cloud screened data) of the SSA data for evaluation. The wavelength dependences of these observations were used to interpolate the values appropriate for the wavelength ranges in the model. The AERONET data were used for model validation with ground-based measurements as well as for the development of a global assimilated AOD (described later).

2.1.2. MISR

[10] MISR on the NASA Terra satellite has been producing AOD measurements globally since February 2000. MISR reports AOD and aerosol type at 17.6 km resolution by analyzing MISR TOA radiances from 16 × 16 pixel patches of 1.1 km resolution [*Diner et al.*, 1998; *Kahn et al.*, 2001]. As the blend of directional and spectral data allow aerosol retrieval algorithms to be used that do not depend on explicit radiometric surface properties, MISR can retrieve aerosol properties over a variety of terrain, including highly reflective surfaces like deserts [*Martonchik et al.*, 2004]. There have been validation efforts by comparing coincident MISR AODs with those obtained from AERONET [e.g., *Martonchik et al.*, 2004; *Kahn et al.*, 2005]. *Kahn et al.* [2005] showed that the uncertainty of instantaneous MISR AODs was around 0.03–0.05, although large uncertainties around 0.05–0.1 have been found for dust event cases [*Martonchik et al.*, 2004; *Kahn et al.*, 2005]. Daily MISR level 2 (version: F06_0017) standard aerosol data products were used with a 1° by 1° grid resolution derived from a spatial resolution of a 17.6 km. Daily mean AODs were compared between the MISR and AERONET data collocated in space and time. Figure 1 shows the comparison of AODs between AERONET and MISR during 2000–2002. The error bars represent the standard deviations (SD) of the AOD ranges. The mean values of temporally and spatially collocated AERONET and MISR AODs were 0.170 and 0.198 respectively. The mean bias and root mean square (RMS) error of MISR AODs to AERONET AODs were 0.028 and 0.196. The positive bias arises mainly for low AOD values (<0.2; see Figure 1b) which also account for more than 80% of the data (Figure 1c). *Abdou et al.* [2005] and *Kahn et al.* [2005] have also shown that MISR AOD is higher than AERONET AOD by values ranging from 0.02 to 0.05. *Kahn et al.* [2005] compared instantaneous MISR AODs with the AERONET AODs, also spatially and temporally collocated. The differences shown in Figure 1 are slightly larger than those shown by *Kahn et al.* [2005] which is expected because the present study compares

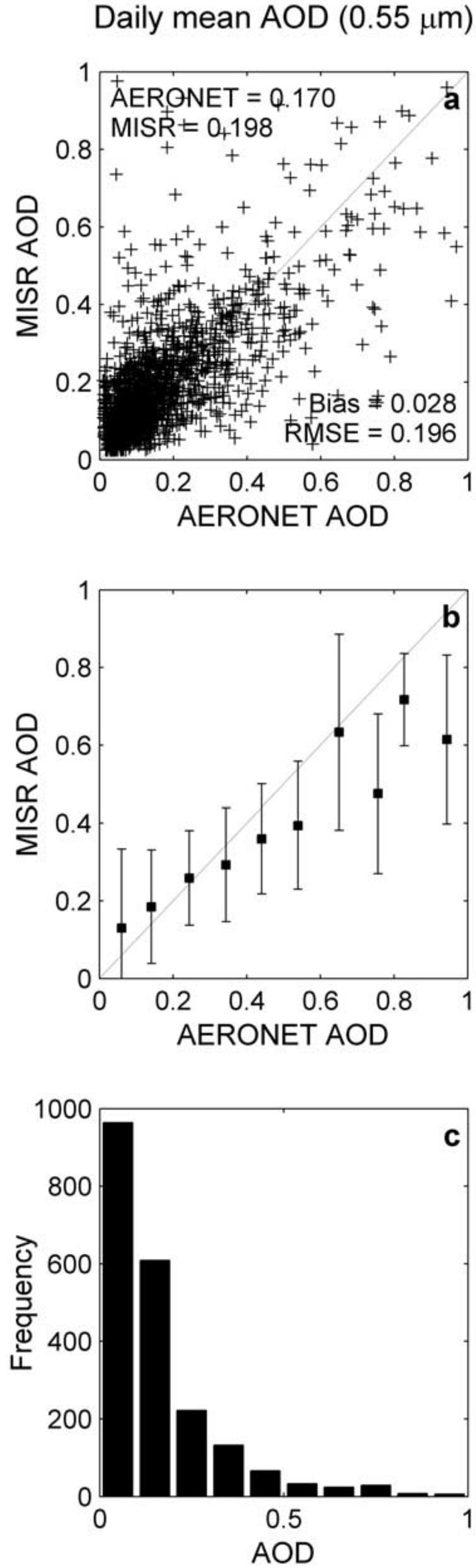

Figure 1. (a) Scatterplot of daily mean AERONET versus MISR AODs during the 2000–2002 period. Here AERONET and MISR represent the total collocated mean AODs. (b) Daily mean AOD comparison with 0.05 interval of AERONET AOD. The error bars represent the mean standard deviation. (c) Numbers of collocated data used for comparison of daily mean AODs.

daily mean values. The satellite samples once a day while AERONET measures every 15 min at a given site. The mean bias in the northern hemisphere (NH) was around 0.034 (with 1743 data points) and is larger than that of the southern hemisphere (SH) which is around −0.021 (with 363 data points) (not shown). Note that the bias of global mean MISR AOD (i.e., including both land and ocean data) can be increased since MISR AODs are overestimated over the ocean, as discussed in Appendix A.

2.1.3. MODIS

[11] For the purpose of assessing the sensitivity to errors in input data, we compare radiation budget values estimated with MISR AOD with those from MODIS_AOD (Moderate Resolution Imaging Spectroradiometer) [*King et al.*, 2003]. The MODIS satellite sensor has provided data on aerosol characteristics since the beginning of the Terra satellite mission in 2000 [*Ichoku et al.*, 2002; *Chu et al.*, 2002; *Remer et al.*, 2002]. The MODIS retrieval uses separate algorithms over land and ocean [*Kaufman et al.*, 1997; *Tanre et al.*, 1997; *Remer et al.*, 2005]. Over vegetated land, MODIS retrieves aerosol optical depth at three visible channels (0.47, 0.55, and 0.66 μm) with high accuracy, i.e., ±0.05 [*Chu et al.*, 2002; *Remer et al.*, 2005]. The Level 3 (collection 4) monthly mean product gives us the monthly statistics based on the original 500 m resolution data. Over the course of a month, MODIS views the same 1° square with a variety of view angles. This study uses the monthly mean data from 2000 to 2002. Figure A1 shows that MODIS AOD is higher than MISR by 0.02 over land and smaller than MISR by 0.02 over ocean, which is similar to results shown by *Abdou et al.* [2005]. In addition to AOD, MODIS provided surface albedo data in 7 bands, as well as in three broad bands, all of which are given in Table 1. MODIS global albedo data retrievals have a 0.05° spatial resolution in a geographic (lat/lon) projection [*Lucht et al.*, 2000; *Schaaf et al.*, 2002; *Roesch et al.*, 2004]. Among the parameters in Table 1, visible (0.4–0.7 μm) and IR (0.7–5.0 μm) surface albedos coincident with the aerosol data are used for solar radiation calculation. The difference between clear-sky and cloudy-sky albedo is not considered. The diurnal surface albedo change is neglected in this study which (based on *Yu et al.* [2004]) can lead to an uncertainty of about 5% (a percent difference) to the monthly average values.

2.1.4. CERES

[12] The Clouds and the Earth's Radiant Energy System (CERES) data were used for the validation of MACR calculations at the TOA. The CERES measures broadband solar and terrestrial radiances at three channels (a shortwave [0.3–5 μm], a total [0.3–200 μm], and an infrared window [8–12 μm]) with a large footprint (e.g., 20 km for CERES/Terra) [*Wielicki et al.*, 1996]. For our validations we employ the Monthly TOA/Surface Averages (SRBAVG) product. The TOA fluxes of CERES (2000–2002 average) are discussed in section 5. The CERES SRBAVG contains monthly (1 product per month) and monthly hourly (24 products per month) TOA fluxes and the cloud properties in a 1° by 1° grid. The products are retrieved by using the recently developed Angular Distribution Models (ADMs) as a function of viewing angle, sun angle, and scene type [*Loeb et al.*, 2003a, 2003b, *Loeb et al.*, 2005]. CERES employs two approaches to temporally interpolate between

Table 1. Data Set Used for MACR Calculation and for Comparison With Other Results

Data Set	Parameters	Period (Temporal Resolution)	Comments
AERONET	AOD: 0.44, 0.5, 0.675, 0.87, and 1.020 μm	2000–2002 (daily and monthly mean)	daily mean: comparison with MISR AOD; monthly mean: integration with MISR AOD and GOCART SSA
MISR (MISR_AM1_CGAS_F06_0017)	AOD: 0.34, 0.38, 0.44, 0.5, 0.675, 0.87, and 1.020 μm	2000–2002 (daily and monthly mean)	resolution: 0.5° × 0.5°; daily mean: comparison with AERONET AOD and validation; monthly mean: MACR simulation
MODIS (MOD08_M3_004)	AOD: 0.47, 0.55, and 0.66 μm (land), at 0.47, 0.55, 0.66, 0.87, 1.24, 1.61, and 2.13 μm (ocean)	2000–2002 (daily and monthly mean)	resolution: 1° × 1°; monthly mean: MACR simulation and comparison with MISR AOD
MODIS (MOD43C1)	surface reflectance over land: visible (0.3–0.7 μm), IR (0.7–5.0 μm), and broadband (0.3–5.0 μm), and 0.47, 0.55, 0.67, 0.86, 1.24 and 2.1 μm.	2000–2002 (16-day mean)	resolution: 0.05° × 0.05°; two broadband (VI and IR) albedos are used for MACR simulation
TOMS	monthly mean total column ozone amount	2000–2002 (monthly mean)	resolution: 1° × 1°
NVAP-NG	total column precipitable water amount (cm)	2000–2001 (daily mean)	data sources: SSM/I, SSM/T-2, ATOVS, Pathfinder PATH A, TMI, and AMSU retrievals; resolution: 0.5° × 0.5°
BSRN	downwelling global, diffuse and direct flux (W m^{-2}) at the surface	2000–2002 (1-min)	fluxes with every 1 min interval (see section 2.2)
GEBA	downwelling global flux (W m^{-2}) at the surface	2000–2002 (monthly mean)	monthly mean fluxes (see section 2.2)
ISCCP-D2	monthly mean cloud fraction and optical depth.	1999–2001 (monthly mean)	monthly mean data; resolution: 2.5° × 2.5°
CERES (SRBAVG)	clear- and all-sky TOA fluxes, cloud properties (cloud optical depth and fraction for low, middle, and high cloud)	2000–2002 (monthly and monthly hourly mean)	resolution: 1° × 1°; data version is SRBAVG Terra FM2 Edition 2D: For baseline calculation, GEO product [*Doelling et al.*, 2006] for flux and clouds (monthly hourly mean data to consider diurnal variation) is used

CERES measurements. The first method (SRBAVG-non-GEO product) interpolates the CERES observations using the assumption of constant meteorological conditions similar to the process used to average CERES ERBE-like data. These fluxes represent an improvement to ERBE-like fluxes due to improvements to input fluxes, scene identification, and directional models of albedo. The second interpolation method (SRBAVG-GEO product) uses 3-hourly radiance and cloud property data from geostationary (GEO) imagers to more accurately model variability between CERES observations. This technique represents a major advancement in the reduction of temporal sampling errors [*Young et al.*, 1998]. CERES SRBAVG defines 4 cloud layers as follows: high (0–300 hPa), upper-mid (300–500 hPa), lower-mid (700–500 hPa) and low (surface to 700 hPa). The monthly hourly mean cloud parameters are used to consider the diurnal variation of clouds described in section 3.4. Water particle radius and ice particle effective diameter are also provided and they are used for retrieving cloud single scattering albedo discussed in section 3.4.

[13] CERES ERBE-like ES-9 product, temporally and spatially averaged fluxes from instantaneous ES-8 products, contains daily and monthly average fluxes for both clear-sky and total-sky scenes in a 2.5° by 2.5° grid. Since daily mean fluxes are not provided by SRBAVG and the SW TOA flux error of ES-9 is relatively small, within 2 W m^{-2} under clear-sky condition [*Loeb et al.*, 2003b], we use ES-9 daily mean clear-sky TOA fluxes, for the model validation of daily mean shortwave fluxes under clear conditions.

2.1.5. ERBE

[14] The Earth and Radiation Budget Experiment (ERBE [see *Ramanathan et al.*, 1989]) provided nearly 5 years of continuous data from the mid-1980s and greatly improved estimate of the global mean energy budget. For this reason ERBE results has been used for model validation for a long time. We also presented ERBE retrieved TOA fluxes for validation and comparison with other results. For the global mean flux comparison we employed the monthly mean data from 1985 to 1989 product (2.5° by 2.5° resolutions). Error estimates showed that global annual mean fluxes could be estimated to have uncertainties of 5∼8 W m^{-2} [*Barkstrom et al.*, 1989; *Rieland and Raschke*, 1991]. ERBE fluxes are frequently compared with CERES values. However, there are several sources of differences between CERES and ERBE: (1) Absolute calibration difference; that is, ERBE had a 2% (1∼1.5 W m^{-2}) calibration while CERES had 1% (0.5∼0.75 W m^{-2}). (2) The field of view (FOV) of ERBE is larger than that of CERES. The resolution of CERES Terra is 20 km at nadir and the resolution of ERBS is 40 km at nadir so that the surface area observed by ERBE is 4 times larger than the area observed by CERES Terra. (3) The different scene identification algorithm, which affects on clear-sky determination. (4) The different angular distribution models (ADM), which affects clear-sky ocean fluxes

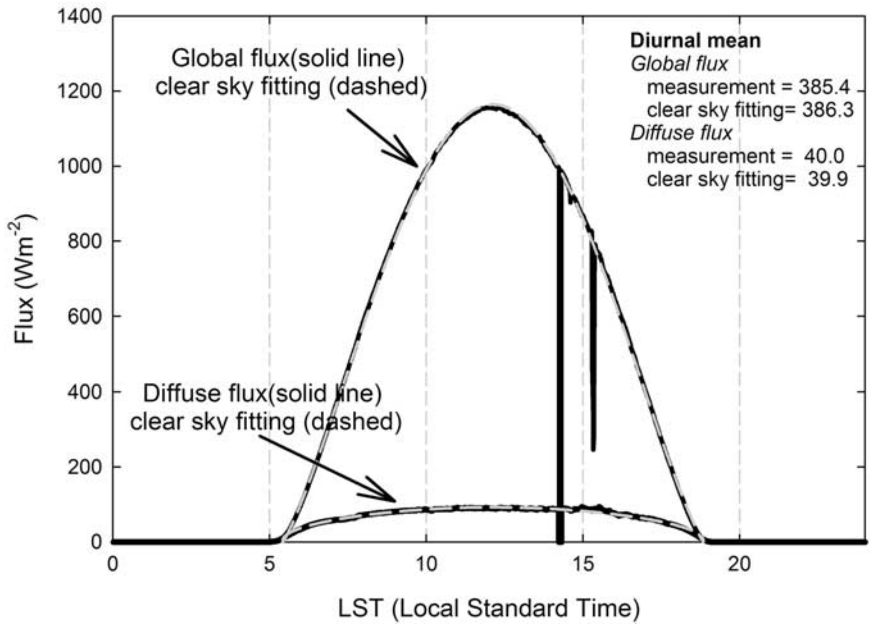

Figure 2. Time series of measured and clear-sky fitted global and diffuse flux at Alice Springs (23.8°S, 133.88°E) for 2 January 1995. Solid lines represent measured global and diffuse flux, and dashed lines represent clear-sky fitted global and diffuse flux.

that causes accuracy limits of diurnal cycle of clear ocean albedo. In general, CERES fluxes are smaller than ERBE values. For all-sky, CERES science team shows the ERBE global annual mean outgoing solar flux at TOA (100.1 W m^{-2} for 1986–1988) is larger than CERES fluxes (96.7~97.8 W m^{-2} for March 2000 to February 2003) by 2.3~3.4 W m^{-2} (http://eosweb.larc.nasa.gov/PRODOCS/ceres/SRBAVG/Quality_Summaries/CER_SRBAVG_Terra_Edition2D.html). The annual zonal mean flux comparison also shows that the ERBE fluxes are systematically larger than the CERES values between 40°S and 40°N for both clear- and all-sky conditions which will be discussed in section 4.5.

2.1.6. ISCCP

[15] The World Climate Research Programme (WCRP) has been collecting infrared and visible radiances obtained from imaging radiometers carried on the international constellation of weather satellites since July 1983 [*Rossow and Schiffer*, 1999]. This compilation comprises the ISCCP (International Satellite Cloud Climatology Project) data set, which provides cloud parameters, such as cloud cover fraction, cloud top pressure and temperature, and cloud optical depth, at a 280 km resolution over the entire globe. The cloud types are defined by three intervals of cloud top pressure, optical depth categories and the phase of the cloud particles; that is, all low (cumulus, stratocumulus and stratus) and middle (altocumulus, altostratus and nimbostratus) cloud types are separated into liquid and ice types, and all high clouds (cirrus, cirrostratus and deep convective) are ice. These 15 cloud types are classified into 4 cloud types: low, middle, high and deep convective clouds. The cloud optical depths were averaged by weighting the optical depth with the individual cloud fraction and normalizing by the total cloud cover under each of the four cloud types. For global solar radiation budget, the ISCCP D2 was used, which is the monthly mean of the ISCCP D1 data set. The monthly mean cloud data was fit to the T42 grid (approximately 2.8° by 2.8°) by interpolation from an equal area grid of 2.5° by 2.5° for the period from January 1999 to September 2001.

2.2. Surface Solar Radiation Data

2.2.1. BSRN

[16] The BSRN operation started in 1992 provides validation data for satellite observations and radiation codes and monitors long-term changes in surface irradiation. At present, there are 35 BSRN stations in operation. The current BSRN uncertainty limit for global and diffuse irradiance is 5 W m^{-2} for a 1 min average [*Ohmura et al.*, 1998]. Clear-sky irradiance was separated from measured irradiance during the day. For this purpose, an empirical fitting algorithm to estimate both the clear-sky total flux and the ratio of diffuse to total flux as a function of solar zenith angle was employed. A detailed description of the method for clear-sky detection is found in the work of *Long and Ackerman* [2000]. Figure 2 shows an example of clear-sky global and diffuse shortwave flux with measured global and diffuse fluxes at Alice Springs (23.8°S, 133.88°E) for 2 January 1995. The solid line represents the observed global (diffuse) fluxes, and the dashed line represents the clear-sky global (diffuse) fluxes retrieved by the clear-sky fitting method. The overall uncertainty of the method is within the accuracy of the model and the pyranometer measurements [*Long and Ackerman*, 2000]. Stations measuring both global and diffuse fluxes were used to apply the clear-sky detection algorithm. For the validation of instantaneous surface flux (every 1 min in Table 1) comparison with MACR, BSRN stations were selected for which both AERONET measurements (every 15 min) of AOD, SSA, and asymmetry factors and water vapor data from radio-

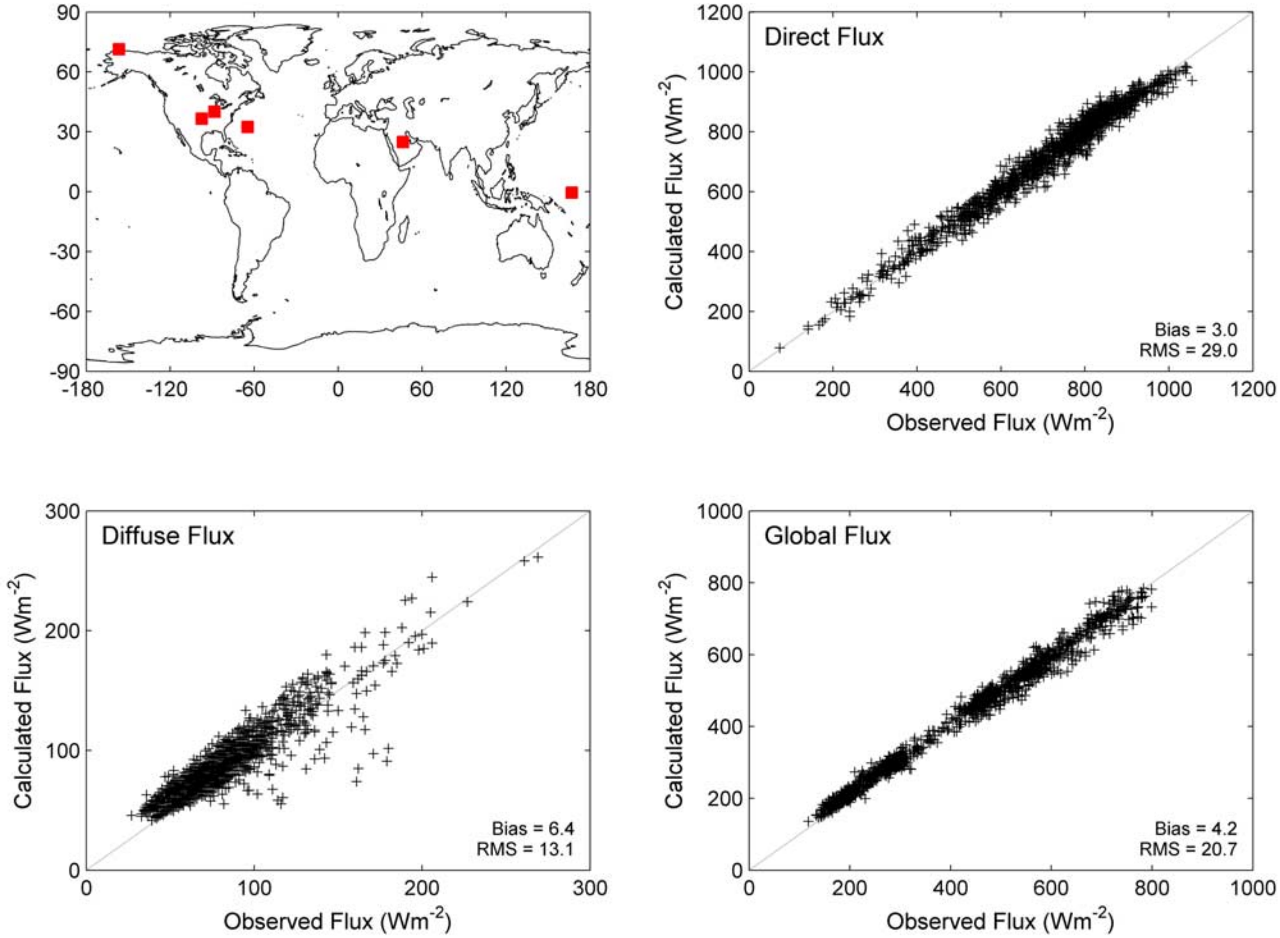

Figure 3. Comparison of instantaneous direct, diffuse and global fluxes (cross) between MACR calculations and BSRN measurements for different solar zenith angles under clear-sky conditions at six BSRN sites (squares).

sondes were available. These multi-instrument criteria significantly reduced the number of suitable stations. The selected stations (Barrow [71.3°N, 156.6°W], Bermuda [32.3°N, 64.8°W], Billings [36.6°N, 97.51°W], Bondville [40.1°N, 88.4°W], Nauru Island [0.5°S, 166.9°E] and Solar Village [24.9°N, 46.4°E]) are given in Figure 3. The daily mean flux comparison using MISR AOD over BSRN sites under the clear-sky condition is given in Figure 4, and the comparisons with different MISR AOD and latitudinal ranges are provided in Figure 5. Detailed discussion is presented in section 4.

2.2.2. GEBA

[17] The Global Energy Balance Archive (GEBA) is another long-term surface solar radiation data set maintained by the World Radiation Data Center [*Gilgen et al.*, 1998; *Gilgen and Ohmura*, 1999]. The GEBA database, created from measurements taken at 1500 surface stations, contains the monthly mean shortwave irradiances since the 1950s. The quality of the GEBA data has been rigorously controlled since the GEBA database was redesigned and updated in 1994 and 1995. Assuming a global mean surface irradiance of 186 W m^{-2}, the relative random errors are approximately 5% of the monthly mean and approximately 2% of the yearly mean with the errors in the monthly and yearly mean corresponding to 10 and 4 W m^{-2} respectively. The GEBA data are widely used for validation of model and satellite remote sensing retrieval algorithm because of the large number of stations and the history of long-term measurements [*Wild et al.*, 1995; *Li et al.*, 1995]. The GEBA data from 2000 to 2002 were matched with BSRN validation periods. Most of the GEBA stations used in this study are located on the Eurasian continent as seen in Figure 5.

3. MACR Description

[18] For the validation study, daily mean values at each station were used. Model inputs were confined by measurements obtained at a given station, but some were interpolated from surrounding grids if the data were not available at a given station, such as cloud optical parameters which are provided on the grid of 1° by 1°. For the global radiation budget calculation, the model was applied on the T42 grid (approximately 2.8° by 2.8° resolution) and run using monthly mean basis inputs. To account for the variations of daylight time and incoming solar radiation at the TOA more accurately, the MACR model needed to be run daily. Monthly mean inputs were interpolated into pseudo-daily values.

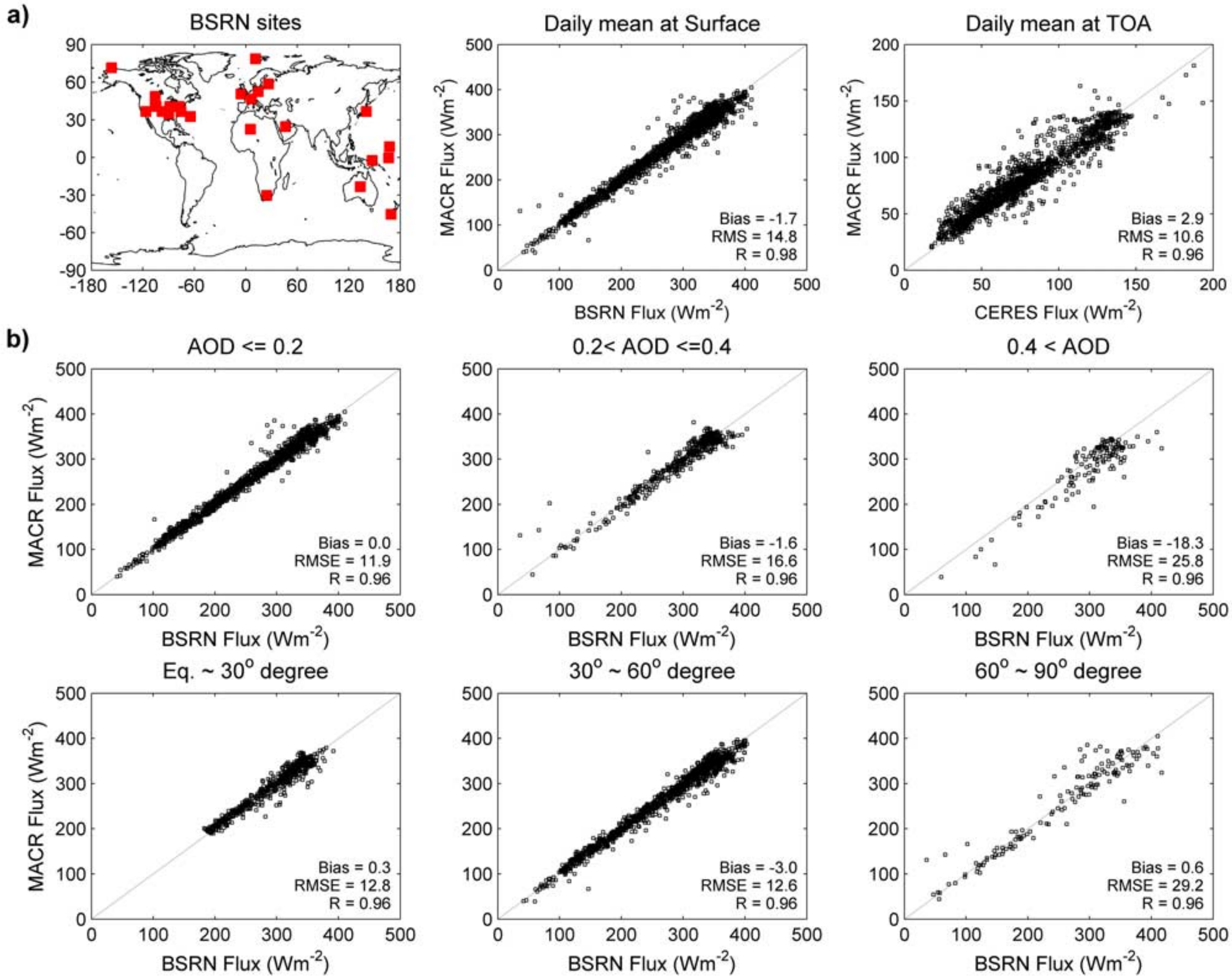

Figure 4. (a) Location of BSRN stations for validation of MACR radiative transfer model during the period from 2000 to 2002. Daily mean flux comparison between BSRN measurements and MACR calculations at the surface and TOA under clear-sky conditions. (b) Daily mean flux comparison between BSRN and MACR with different MISR AOD (0∼0.2, 0.2∼0.4, and AOD > 0.4) and latitudinal (equator ∼30°, 30°∼60°, and 60°∼90°) ranges at the surface.

3.1. Description of Model

[19] MACR was developed as a 1-D column model at the Center for Clouds, Chemistry, and Climate (C^4), Scripps Institution of Oceanography and validated extensively with INDOEX data [*Podgorny et al.*, 2000; *Podgorny and Ramanathan*, 2001; *Ramanathan et al.*, 2001a]. The model accounts for the multiple scattering and absorption by individual aerosol species, cloud droplets, air molecules, and reflections from the surface. The model uses 25 bands to cover the solar spectrum from 0.25 to 5.0 μm with 50 layers [*Vogelmann et al.*, 2001]. Recently the MACR model has been updated to produce global gridded simulations using observational input data, such as aerosol optical parameters, total ozone amount, precipitable water, surface albedo, surface altitude, and cloud parameters.

[20] The main advantage of the MACR model for solving the radiative transfer equation is its accurate calculation of the atmospheric fluxes values as compared to those values obtained with two-stream approximations for both clear and all skies [e.g., *Barker et al.*, 2003; *Halthore et al.*, 2005]. MACR is capable of using 3-D aerosol distribution which is required for more accurate treatment of aerosol-cloud radiative interaction [*Podgorny and Ramanathan*, 2001].

3.2. Atmospheric Absorption and Surface Albedo

[21] The correlated k distributions (referred to as CK) [e.g., *Lacis and Oinas*, 1991; *Fu and Liou*, 1992; *Kato et al.*, 1999] are used to incorporate gaseous absorption by water vapor, ozone, oxygen, and carbon dioxide, which require a total run of 3132 monochromatic calculations per shortwave broadband. The CK is generated for 50 layers and 25 spectral regions on the basis of the 2000 version of high-resolution transmission molecular absorption database (HITRAN 2000 database). The water vapor continuum absorption based on the algorithm given by *Clough et al.* [1989] is also incorporated in the CK because of the increasing importance of water vapor continuum absorption in shortwave radiative transfer computations [*Stephens and Tsay*, 1990; *Vogelmann et al.*, 1998; *Fu et al.*, 1998].

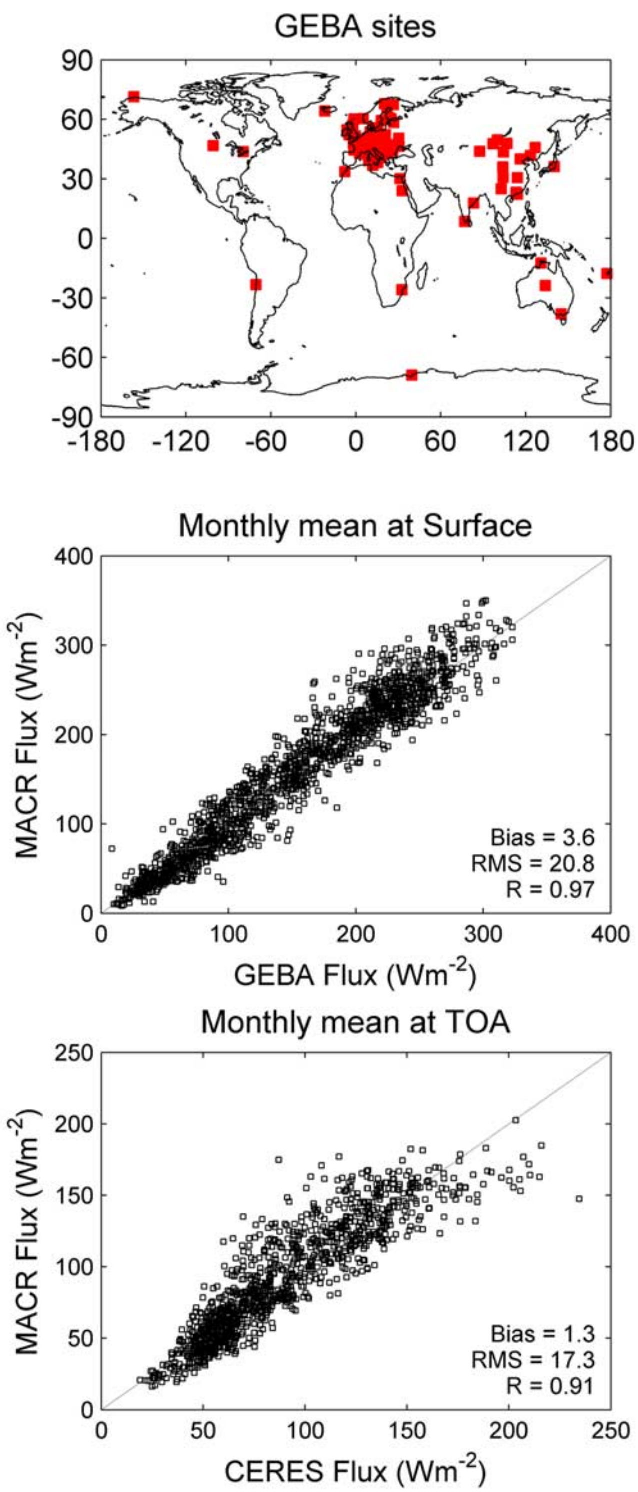

Figure 5. Location of GEBA stations for validation. Monthly mean flux comparison between GEBA measurements and MACR calculations at the surface and TOA under all-sky conditions.

[22] For the atmospheric gases, the vertically integrated amount of ozone from 2000 to 2002 was derived from TOMS. The Water Vapor Project (NVAP-Next Generation) total column water vapor data sets from 2000 to 2001, obtained from the NASA Langley Research Center Atmospheric Sciences Data Center, was used [*Randel et al.*, 1996]. NVAP-NG has merged retrievals and products from low-Earth orbiting satellite platforms and created a global, twice-daily, 0.5° resolution, 5 layers water vapor product for the years 2000 and 2001 [*Forsythe et al.*, 2003; *Vonder Haar et al.*, 2003]. Input data included three SSM/I, ATOVS, TOVS, and new instruments that were not used for NVAP, which were the Advanced Microwave Sounding Unit-B (AMSU-B), Special Sensor Microwave/Temperature-2 (SSM/T-2) as well as the Tropical Rainfall Measuring Mission Microwave Imager (TMI). Both ozone and water vapor inputs are a function of time and location. The surface orography effects were taken into consideration by removing air and any cloud below elevated surfaces. To investigate the uncertainty of MACR atmospheric gaseous absorption, we compared the MACR estimated fluxes without both aerosol and cloud (only atmospheric gases and Rayleigh scattering) with those of line-by-line models (LBL) in the work by *Halthore et al.* [2005]. For the comparison, we carried out MACR simulation keeping the same gas amount and profile in the work by *Halthore et al.* [2005]. At the surface the mean global (direct + diffuse) flux differences between MACR and the five LBL models are 0–1 W m^{-2} with the RMS error of 1–2 W m^{-2} at 75° solar zenith angle, while 1–2 W m^{-2} with the RMS error of 3–5 W m^{-2} at 30° solar zenith angle (not shown).

[23] The ocean surface albedo adopted for this study was the ocean albedo scheme given by *Briegleb et al.* [1986], which was based on the work of *Briegleb and Ramanathan* [1982]. The ocean surface albedo, expressed by the cosine solar zenith angle, yielded 2.5% of the surface albedo when the sun was overhead and more than 20% of the albedo for larger (≈80°) solar zenith angles. In addition to the land surface and sea ice albedo from the MODIS described in section 2.1, the surface albedo from European Centre for Medium-Range Weather Forecasts (ECMWF) surface solar radiation reanalysis (1998–2001 mean), which was based on satellite-derived values [*Preuß and Geleyn*, 1980; *Geleyn and Preuß*, 1983], was obtained by the ratio of upward to downward broadband flux ($F^{\uparrow}/F^{\downarrow}$), was also used to investigate the effect of surface albedo on the global radiation budget.

3.3. Aerosol Parameters

[24] The input parameters for aerosol properties in radiative transfer calculation are AOD, SSA, and asymmetry factor. The Angstrom exponent was adopted to account for the wavelength dependence of each aerosol parameter as described in Appendix A. The scattering angle after a photon collides with an aerosol particle was determined by the Henyey-Greenstein phase function. Since *Ramanathan et al.* [2001a] showed the typical boundary layer aerosol over tropical ocean is up to 2 km and elevated aerosol layer is up to 3–4 km by lidar measurement during INDOEX, the vertical distribution of aerosols was assumed to be homogeneous from the surface to 3.4 km in the tropics (30°S–30°N), and homogeneous to 2 km in the extratropics [*Chung et al.*, 2005]. Above this height, the aerosol concentration exponentially decreased. *Liao and Seinfeld* [1998a] showed that the vertical shape of aerosol distribution is unimportant only when aerosols (such as dust) are

Table 2. Uncertainties in Annual Mean Fluxes and Aerosol Forcing at the Surface and TOA due to Estimated Errors in Input Parameters[a]

Parameters	TOA Flux	TOA Forcing	Surface Flux	Surface Forcing
Flux and forcing for standard case	61.2	−5.0	224.1	−9.3
AOD (0.18 ± 0.02)	0.7	0.6	1.5	1.4
SSA (0.95 ± 0.03)	0.8	0.8	1.5	1.2
PW (3.0 ± 0.3)	0.2	0.0	1.3	0.2
Ozone (300 ± 30)	0.2	0.0	0.4	0.2
Albedo (0.15 ± 0.02)	4.5	0.4	0.5	0.2
All aerosols are confined up to 1 km from surface (clear sky)	0.0	0.1	0.1	0.0
All aerosols are from 3 to 4 km (clear sky)	0.3	0.3	0.0	0.2
Cloud fraction (0.5 ± 0.05)	2.9	0.3	4.3	0.2
Cloud optical depth (thin: 5.0 ± 0.5)	1.9	0.2	2.6	0.2
Cloud optical depth (thick: 20.0 ± 2.0)	2.2	0.0	2.8	0.2
All aerosols are confined up to 1 km from surface (all-sky)	0.3	0.2	0.0	0.1
All aerosols are from 3 to 4 km (all-sky)	0.3	0.3	0.0	0.0

[a]The test was conducted for clear-sky case except for the change in cloud fraction and optical depth. For the aerosol-cloud interaction, the sensitivity test for different aerosol profiles was run at both clear and all-sky cases. Units are W m^{-2} for flux (net fluxes at the surface while upwelling fluxes at TOA) and aerosol forcing.

below 3 km and clouds are not present. *Liao and Seinfeld* [1998b] also showed that TOA forcing is highly dependent on vertical distribution of aerosol in the presence of cloud layers. For this reason, we simulate the MACR with two different aerosol vertical profiles; first, all aerosols are trapped within 1 km height from the surface, and second, all aerosols are trapped between 3 and 4 km height. For these simulations, altitude-dependent relative humidity effects are not included in the aerosol properties. The results of sensitivity tests are provided in Table 2, while those of global runs are provided in Table 3.

3.4. Cloud Parameters

[25] *Podgorny and Ramanathan* [2001] used the MACR 3-D cloud schemes to investigate the effects of 3-D cloud geometry on the regional and diurnal averaged shortwave aerosol radiative forcing. They found these effects to be less important than the uncertainties in specifying aerosol SSA or cloud fraction. Cloud optical thickness and fraction as a function of cloud type were the important cloud parameters with respect to the all-sky aerosol radiative forcing. The climatology of cloud optical depth and cloud fraction obtained from ISCCP and CERES global cloud data sets are implemented in MACR model. On the basis of the validation studies to be described later, we adopted CERES cloudiness as our baseline case. We characterized the cloud fraction, optical depth and other cloud parameters under three categories, i.e., low (cloud top pressure, $P_c > 680$ hPa), middle ($440 < P_c < 680$ hPa), and high ($P_c < 440$ hPa) clouds.

[26] Satellite derived cloud fraction implicitly assumes are no overlap of clouds between layers. Basically the retrieval scheme derives the cloud fraction viewed by the scanning radiometers, and characterizes the cloud as low, middle or upper level cloud. In principle, it is a finite probability that there are middle- and low-level clouds beneath a higher-level cloud. On the other hand, when the satellite characterizes a scene as low-level cloud, it is safe to assume there are no middle or upper level clouds (with the exception of optically thin clouds) above this low cloud. Thus effectively, the derived cloud fraction for upper level

Table 3a. Global Annual Mean Fluxes, Aerosol Radiative Forcing (ARF) and Cloud Radiative Forcing (C_f) Estimated With Different Aerosol and Cloud Data for MACR Calculations Under All-Sky Conditions for the TOA Flux (TOA), Atmospheric Solar Absorption (ATM), and Surface Flux (SFC)[a]

Case	Flux TOA	Flux ATM	Flux SFC	ARF TOA	ARF ATM	ARF SFC	C_f	Sources
MACR_BL	98.9	79.3	163.6	−3.0	4.4	−7.4	−47.5	baseline case for present study: MISR monthly mean AOD, CERES GEO monthly hourly mean cloud (see section 2.1 for CERES data description), MODIS surface albedo, and standard aerosol profile (see section 3.3)
MACR_AER_A	99.1	78.9	163.8	−3.2	3.9	−7.2	−47.4	same as baseline case (MACR_BL) except for aerosol < 1 km
MACR_AER_B	98.6	79.4	163.8	−2.7	4.4	−7.2	−46.9	same as baseline case (MACR_BL) except for aerosol between 3 and 4 km
MACR_M	99.1	79.5	163.3	−3.0	4.1	−7.1	−47.7	same as baseline case (MACR_BL) except for CERES monthly mean cloud
MACR_ISCCP_M	98.1	79.1	164.7	−3.0	3.9	−6.9	−47.2	MISR AOD, ISCCP-D2 monthly mean cloud, ECMWF surface albedo, and standard aerosol profile
MACR_ MODIS_ISCCP _M	98.3	79.5	164.1	−3.2	4.3	−7.5	−47.2	MODIS AOD, ISCCP-D2 monthly mean cloud, ECMWF surface albedo, and standard aerosol profile
MACR_MISR_AERO_ISCCP_M	97.7	78.8	165.4	−2.6	3.6	−6.2	−47.6	MISR+AERONET integrated AOD, ISCCP-D2 monthly mean cloud, ECMWF surface albedo, and standard aerosol profile

[a]Units are given in W m^{-2}.

Table 3b. Same as Table 3a but for Clear-Sky Conditions

Case	Flux			ARF			Sources
	TOA	ATM	SFC	TOA	ATM	SFC	
MACR_BL	51.4	72.1	218.3	−5.9	4.8	−10.7	baseline case for present study: MISR AOD, MODIS surface albedo (see section 2.1), and standard aerosol profile (see section 3.3)
MACR_AER_A	51.6	72.2	218.1	−6.0	4.9	−11.0	same as baseline case (MACR_BL) except for aerosol < 1 km
MACR_AER_B	51.7	71.8	218.4	−5.9	4.8	−10.7	same as baseline case (MACR_BL) except for aerosol between 3 and 4 km
MACR_ECMWF	50.9	71.9	219.0	−5.8	4.7	−10.5	same as baseline case (MACR_BL) except for ECMWF surface albedo
MACR_MODIS	51.6	72.2	218.1	−6.0	4.9	−10.9	same as baseline case (MACR_BL) except for MODIS AOD
MACR_MODIS_ECMWF	51.1	72.2	218.5	−6.0	5.0	−11.0	MODIS AOD, ECMWF surface albedo, and standard aerosol profile
MACR_MISR_AERO_ECMWF	50.1	71.4	220.4	−5.0	4.1	−9.1	MISR+AERONET integrated AOD, ECMWF surface albedo, and standard aerosol profile

should be close to reality, whereas, the low cloud fraction is biased toward lower values because of the potential masking (or shadowing) of low clouds by middle or upper level clouds. With respect to biases in satellite derived optical depth, however, the situation is reversed. The low cloud optical depth should be closer to the true optical depth, whereas, the optical depth of upper and middle level clouds may be contaminated by overlapping low clouds.

[27] In order to account for such vertical cloud overlap, we assume the random overlap scheme proposed by *Chen et al.* [2000], which is described briefly below. Within each grid (of say 100 km by 100 km) the satellite derives cloud fractions and optical depths at three effective levels. We assume that a random overlap exists when the upper level cloud optical depth is greater than lower-level cloud optical depth. The rationale is that, upper level cirrus cloud optical depths are normally lower than low-level water cloud optical depths. When this criterion is met, we assume the low clouds and middle-level clouds are randomly overlapped with the high clouds. For example, if the low cloud fraction is 0.2, we assume 20% of low clouds occur beneath the middle clouds, 20% occur beneath the high cloud and 20% occur in the clear-sky portions. However, the total amount of lower-level cloud is renormalized such that the total sky covered by clouds is same as the satellite derived cloud fraction. We then scale down the optical depths of the middle and upper level clouds such that the total optical depth (weighted by cloud fraction) is conserved. The random cloud overlap scheme leads to eight different cloud configurations: clear sky, low-level, midlevel, midlevel over low-level and high-level, high-level over midlevel, high-level over low-level, and high-level over midlevel and low-level cloud. Deep convective clouds are explicitly taken into account.

[28] Cloud SSA (as a function of wavelength) and asymmetry factors have been computed using Optical Properties of Aerosols and Clouds (OPAC) software, since OPAC provides six water clouds (effective radius ranges from 4.0 to 12.68 μm) and three ice clouds (effective radius ranges from 34 to 92 μm) which are given for up to 61 wavelengths between 0.25 and 40 μm [*Hess et al.*, 1998]. The SSAs of water clouds range from 0.984 to 0.95 at 1.6 μm, while SSAs of ice clouds range from 0.845 to 0.928 at 1.6 μm. CERES cloud effective radii of low, middle and high cloud were used to retrieve cloud SSAs from OPAC. These cloud SSAs are similar with those used by *Minnis et al.* [1998]. Henyey-Greenstein phase function and the delta function adjustments of cloud optical depth, cloud SSA, and cloud asymmetry factor were incorporated to account for the cloud scattering [*Joseph et al.*, 1976]. The external mixing approximation was used for the interstitial aerosol because of the lack of information on the mixing properties of absorbing aerosols and cloud drops.

[29] In addition to cloud optical properties, the diurnal variations of clouds were taken into account. We later show that the diurnal variation of clouds have a substantial impact on the monthly mean radiation budget.

4. Evaluation of the Radiation Budget Estimates

4.1. Overall Evaluation Strategy

[30] The evaluation results shown here adopt the following strategy. First we compare with instantaneous clear-sky fluxes at the BSRN sites with collocated AERONET aerosol observations and radiosonde water vapor data; that is, the comparison with BSRN is undertaken at times (±15 min) to coincide with successful AERONET data (AOD, SSA, and asymmetry factor) as well as radiosonde data. This step enables us to quantify the uncertainties in MACR estimates of surface radiation fluxes. We are assuming that radiosonde water vapor data and AERONET aerosol parameters are of sufficient accuracy that they are not the major source of errors in calculated fluxes. We did not include TOA fluxes at this step because of the disparity in spatial scales of CERES TOA fluxes (typically 50 to 100 km at the pixel level) and that of the input data from AERONET and Radiosonde (from few hundred meters to few kilometers). Second, we repeat the comparison with daily mean fluxes

Table 4a. Global Annual Mean Solar Radiation Budget Under All-Sky Conditions Derived From Different Data and Methods: ISCCP-FD [*Zhang et al.*, 2004], ERBE [*Li and Leighton*, 1993], AMIP-II [*Wild*, 2005; *Wild et al.*, 2006], and IPCC-2001 [*IPCC*, 2001] and IPCC-AR4 [*Wild et al.*, 2006][a]

Case	TOA: F_r (Albedo)	ATM	SFC	C_f	Period	Sources
MACR_BL	98.9 ± 4 (28.9 ± 1.2)	79.3 ± 5	163.6 ± 6	−47.5 ± 4	2000–2002	present study: calculation (baseline case[b]: see MACR_BL in Table 3a)
CERES	97.1 (28.4)	-	171.3	−46.5	Mar 2000 to Dec 2002	present study: observation at TOA[c] [*Loeb et al.*, 2003a, 2003b, 2005], surface flux is based on model calculation
CERES	97.8 (28.6)	-	-	-	Mar 2000 to Feb 2003	*Doelling et al.* [2006]
ERBE	101.3 (29.6)	-	157	−48	1985–1989	observation at TOA; surface fluxes are based on model calculation [*Li and Leighton*, 1993]
IPCC 2001	107 (31.3)	67	168	−50	-	*IPCC* [2001], *Kiehl and Trenberth* [1997]
ISCCP-FD	105.7 (30.9)	70.9	165.2	−50.3	1985–1989	*Zhang et al.* [2004]: model calculation
AMIP-II	106 (31.0)	74	162	−46	1979–1996	*Wild* [2005]: mean of 20 GCMs

[a]F_r represents the reflected flux at TOA and albedo is given in percent (%). C_f presents the cloud radiative forcing (W m^{-2}) at TOA. Insolation at TOA is assumed to be 1367 W m^{-2} yielding a global annual mean insolation of 341.8 W m^{-2}.
[b]For baseline case, we used MISR monthly mean AOD, CERES monthly hourly mean clouds (data set: SRBAVG Terra FM2 Edition 2D, GEO product), MODIS surface albedo (MOD43C1), and standard aerosol profile (see section 3).
[c]For CERES TOA flux, SRBAVG GEO TOA flux was used (see section 2.1).

for clear skies at surface as well as at TOA using respectively BSRN and CERES daily mean fluxes. This step enables us to quantify the errors in diurnal mean clear-sky fluxes. In addition, by comparing the errors between the first step and this, we are able to understand the errors in using diurnally averaged input parameters. Third, we compare the monthly mean fluxes using GEBA data sets. The reason for switching from BSRN to GEBA fluxes for this portion of the evaluation is that GEBA covers a much broader range of latitude and longitude zones and thus enables us to make a better assessment of global mean uncertainties. Last, we compare zonal and global annual mean comparisons with CERES TOA fluxes to get an overall estimate of the errors in our estimates of the global mean solar radiation budget. Even though CERES and ERBE surface radiation values are provided in Table 4, the surface net flux comparison has not been undertaken since they are not directly measured values. Basically our strategy is opportunistic in that it makes optimum use of the available data sets to get a handle on the overall uncertainty of our new estimates of solar radiation budget.

4.2. BSRN Stations: Instantaneous and Daily Mean Fluxes at the Surface

[31] We chose BSRN stations coincident with AERONET and radiosonde sites for the period from 2000 and 2002. This period was selected because the CERES TOA fluxes and cloud data were available only beginning 2000. The daily total ozone amounts from TOMS measurements (1° by 1° resolution) were employed. Only 6 BSRN stations survived our filtering process and are shown in Figure 3. We will first focus on the mean bias and discuss later the RMS errors.

[32] Figure 3 compares instantaneous direct, diffuse, and global (direct plus diffuse) fluxes at the surface between BSRN and MACR under clear-sky conditions. At the surface MACR overestimates the direct and global flux by 3.0 and 4.2 W m^{-2}; that is, the simulated fluxes agree with the observed values within 1% which is within the accuracy of the radiometers (about 0.5 to 1% for the pyrheliometer used for the direct flux and about 1 to 2% for the pyranometers used for the global diffuse fluxes). The error in the diffuse fluxes however exceeds 5% (about 6.4 W m^{-2}).

Table 4b. Same as Table 4a but for Clear-Sky Conditions[a]

Case	TOA: F_r (Albedo)	ATM	SFC	Period	Sources
MACR_BL	51.4 ± 2 (15.0 ± 0.6)	72.1 ± 3	218.3 ± 4	2000–2002	present study: calculation (baseline case[b]: see MACR_BL in Table 3b)
CERES	50.6 (15.2)	-	214.9	Mar 2000 to Dec 2002	present study: observation at TOA[c] [*Loeb et al.*, 2003a, 2003b, 2005]; surface flux is based on model calculation
ERBE	53.3 (15.5)	-	209	1985–1989	*Li and Leighton* [1993], *Li et al.* [1997]; surface flux is based on model calculation
IPCC 2001	57 (16.7)	60	225	-	*IPCC* [2001], *Kiehl and Trenberth* [1997]
ISCCP-FD	55.4 (16.2)	68.0	218.4	1985–1989	*Zhang et al.* [2004]: model calculation
AMIP-II	52 (15.2)	67	222	1979–1996	*Wild et al.* [2006]: mean of 20 GCMs
IPCC-AR4	54 (15.8)	69	219	-	*Wild et al.* [2006]: mean of 14 GCMs

[a]F_r represents the reflected flux at TOA and albedo is given in percent (%). C_f presents the cloud radiative forcing (W m^{-2}) at TOA. Insolation at TOA is assumed to be 1367 W m^{-2} yielding a global annual mean insolation of 341.8 W m^{-2}.
[b]For baseline case, we used MISR monthly mean AOD, CERES monthly hourly mean clouds (data set: SRBAVG Terra FM2 Edition 2D, GEO product), MODIS surface albedo (MOD43C1), and standard aerosol profile (see section 3).
[c]For CERES TOA flux, SRBAVG GEO TOA flux was used (see section 2.1).

The overestimation of the diffuse fluxes is in part due to the effect of the shading ball (used to shade the direct sunlight from the sensor) which can be as large as 5 W m^{-2} [e.g., *Ramana and Ramanathan*, 2006]. In addition to the effect of the shading ball, IR loss of the thermopile detector in the pyranometer, even when shaded, can be a significant source of correctable error in diffuse measurement [*Dutton et al.*, 2001]. An algorithm, developed for determining the offset error based on the sky net IR forcing, found this error, on the average, to be within ±4 W m^{-2} for ventilated pyranometers. If we correct for the fluxes blocked out by the shading ball, the MACR-BSRN bias of diffuse flux would be well within the uncertainties of direct/global fluxes. Nevertheless, since all three components (direct, diffuse and global) are overestimated by MACR, it is possible that the model is underestimating atmospheric solar absorption by about 3 W m^{-2} or TOA albedo by about 1% (equivalent to 3 W m^{-2} TOA reflection).

[33] Figure 4a compares the diurnal mean clear-sky solar fluxes, at the surface and at TOA, between observations and MACR. These estimates use MISR AODs as input. We switched from AERONET to MISR AODs for two reasons: the use of MISR AODs allows us to use more BSRN sites (e.g., compare BSRN sites in Figure 3a with those shown in Figure 4a); the use of satellite AODs ensures compatibility between the temporal and spatial scales of AODs and CERES TOA fluxes. At the surface the MACR–BSRN bias (1.7 W m^{-2}) is similar to that shown in Figure 3a, thus suggesting no substantial increase in error due to diurnal averaging. For the reflected solar flux at TOA, MACR overestimates it by around 3 W m^{-2} with the RMS error of about 10.6 W m^{-2}. Again the bias in the TOA fluxes is well within the CERES uncertainties.

[34] Now we will focus on the much larger RMS errors in Figures 3 and 4. Examining first Figure 4b, we note that the bias errors increase significantly for AODs larger than 0.2, which is consistent with the AOD uncertainties shown in Figure 1. Thus one source of the larger RMS errors in Figures 3 and 4 is the uncertainty in measured aerosol parameters for larger AODs. Next we also see that the errors (both bias and RMS) are larger for high latitudes. The high-latitude discrepancies may arise from relatively large uncertainties in MISR AOD retrievals due to the larger uncertainties in cloud screening at high latitudes [*Di Girolamo and Wilson*, 2003].

[35] To investigate other sources of RMS errors, we first examined the uncertainty of clear-sky identification method used for retrievals of diurnal mean clear-sky fluxes (BSRN). We chose the collocated observed fluxes with clear-sky fitted data. The daylight absolute mean differences between observed and clear-sky fitted fluxes were less than 2–3 W m^{-2}. Next we examined the AERONET AOD variations during the day, which was in the range of 0.05–0.06 at the BSRN stations. The importance in the diurnal variation of AOD is tested versus using the AOD diurnal average which is found to be less than 1 W m^{-2}. To investigate the uncertainty due to the AOD and SSA retrieval errors, we conducted a sensitivity test with the known errors in AERONET AOD (±0.02) and SSA (±0.03) [*Dubovik et al.*, 2000]. The maximum uncertainty of the diurnal mean flux at the surface was around 4 W m^{-2}. The uncertainty in column water vapor amount and total ozone amount (assuming they are 10%) causes 1–2 W m^{-2} uncertainty of the incoming surface fluxes (The TOA fluxes are highly dependent on ground albedo as well as AOD and SSA. The uncertainty of TOA flux was around 4–5 W m^{-2} because of a 10% error of ground albedo, while the surface net flux change was within 1 W m^{-2}). Another source of discrepancy is due to spatial sampling errors, since we used grid mean values as model inputs to compare calculated fluxes with ground-based single-point measurements. *Li et al.* [2005] showed that the sampling errors are about 4–5 W m^{-2} for a model grid size of 100 × 100 km^2 when compared with ground observations. Among them, the largest uncertainty in radiative forcing estimates at both the surface and TOA comes from the uncertainty of AOD and SSA. However, the largest uncertainty for flux calculation is caused by the uncertainty of cloud fraction at the surface and that of albedo at TOA in Table 2. If we assume that the various sources of errors discussed above are uncorrelated, the cumulative contribution to the random error is about 7–9 W m^{-2}, compared with the 11 to 15 W m^{-2} RMS errors shown in Figure 4a (surface and TOA). The balance is most likely due to variations in aerosol vertical distribution contamination of fluxes by thin cirrus clouds (which are not easy to detect without LIDARs), among other possibilities. However, the fact that the mean bias in all of the cases shown in Figures 3 and 4 are much smaller than the RMS errors reassures us that the errors are in fact random and cancel out in the mean. In summary, we deduce that the accuracy of MACR and the daily input data are sufficient to make an estimate of the solar radiation budget for the planet.

4.3. GEBA Stations: Monthly Mean Surface Fluxes for Average Cloud Conditions

[36] We extend the MACR-observations comparison to GEBA stations which are more uniformly distributed around the globe. However, GEBA data are available for only monthly mean conditions and furthermore ground based aerosol data from AERONET are available for only 3 stations. Hence we use monthly mean MISR AODs. The detailed integration method for global aerosol optical properties such as SSAs is described in Appendix A. For all-sky flux calculation CERES cloud fraction, optical depth, and effective radius are used as described in section 3.4. Only all-sky global flux comparisons were made, since it is not possible to filter clear-sky data from monthly mean solar fluxes.

[37] Figure 5 shows monthly mean global flux comparison at the surface and TOA over GEBA sites for 2000–2002. For TOA flux comparison, CERES data over GEBA sites are used. The uncertainties in GEBA monthly mean fluxes are in the range of 10 W m^{-2} [*Gilgen et al.*, 1998]. At the surface the mean bias is around +3.6 W m^{-2}, and the RMS error is as large as 21.0 W m^{-2}. At the TOA the mean bias is smaller (+1.3 W m^{-2}), and the RMS error is slightly smaller (17.3 W m^{-2}). At the surface the mean bias of about +9 W m^{-2} over low latitude (equator to 30°) was much larger than those of midlatitude (30–60°) and high latitude (60–90°) around 1.7 and −1.5 W m^{-2} respectively. The large bias over lower latitudes might be partially caused by underestimated MISR AOD, especially for biomass burning

aerosols, since the largest errors are shown at high surface flux values, i.e., mainly cloud free cases. However, the bias is almost independent of AOD values. The mean biases showed the same patterns at TOA, suggesting that the most likely cause was the uncertainties in clouds, which is indeed consistent with the sensitivity results shown in Table 2. These results are also consistent with large differences of MACR-CERES cloud radiative forcings discussed later in section 5.3. Other sources for the discrepancies are the spatial sampling errors in model input parameters [e.g., *Li et al.*, 2005] and the temporal sampling errors arising from the use of monthly mean input data.

[38] For more quantitative values of the uncertainty in monthly mean MACR estimates, we conducted sensitivity tests by changing aerosol and cloud parameters. Table 2 presents uncertainties of the annual mean flux and aerosol forcing due to errors of input parameters at the surface and TOA. For the same input errors, the TOA reflected flux has a larger percent error than the surface flux. An input error of 10%, results in an overall uncertainty of the TOA flux in the range of 0.3 to 7.5%, while at the surface the uncertainties of MACR estimated fluxes are within 2.0%. For the aerosol radiative forcing (ARF), however, both the TOA and the surface forcing have large uncertainties around 15–16% due to given errors of AOD and SSA for clear sky. In addition, the TOA forcing is extremely sensitive to surface albedo and aerosol vertical distributions. For the all-sky total aerosol TOA forcing, the 10% error of surface albedo could induce an uncertainty around 8–9%, whereas the uncertainties of surface forcing are within 2.5% error. The change of aerosol vertical profile could induce up to a 7–9% error for the TOA forcing in the presence of the clouds, while the error ranges from 2 to 6% under clear-sky conditions. These results are consistent with the study of *Podgorny and Ramanathan* [2001] which showed an almost twofold increase in the TOA forcing when aerosols were above the clouds compared with aerosols below the clouds.

4.4. CERES and ERBE TOA Fluxes

[39] This sub section is organized as follows. We will first describe the sensitivity to the source of cloud data (ISCCP versus CERES) and to temporal averages over diurnal and daily timescales. For this purpose we consider one month (January) as opposed to annual mean. This is followed by annual mean conditions for which we explore the sensitivity to aerosol and cloud data and compare these with ERBE and CERES radiation budget data. For both these cases we will consider zonal means as well as global mean values.

4.4.1. Sensitivity to Cloud Data and Diurnal/Daily Cloud Variations

[40] Figure 6 displays the sensitivity results for zonal means (the curves) and for global means (the numbers within parentheses). We show several cases of model results: (1) MACR_BL (MACR baseline case), which adopts monthly hourly mean cloud data (from the CERES) for each hour of the day with nonzero insolation; (2) MACR_M (same as baseline case except for CERES monthly mean cloud), which adopts the diurnal average (over day time values) for monthly mean values; (3) MACR_ISCCP_MH (MISR AOD, and every 3-hourly ISCCP-D2) which adopts daily mean clouds for every 3 hours; and (4) MACR_ISCCP_M (MISR AOD, and monthly ISCCP-D2) which adopts monthly and diurnally averaged cloud. Our standard for assessing the quality of the data is its ability to simulate the observed CERES radiation budget which is also shown in Figure 6. The individual sensitivity studies are summarized below.

4.4.1.1. Cloud Data

[41] By comparing MACR_M with MACR_ISCCP_M, we investigate the sensitivity to input data sets. We note from the global mean values, the reflected solar flux using MACR_ISCCP_M is smaller than that using MACR_M by about 8 W m^{-2} for oceans, 7 W m^{-2} for land and 8 W m^{-2} for ocean + land. The observed fluxes are roughly midway between the two model cases.

4.4.1.2. Diurnal Variations

[42] Focusing next on diurnal averaging, we compare MACR_BL with MACR_M. The differences are systematic in that, over land the use of hourly data increases reflected solar flux by about 4 W m^{-2}, while over the ocean it decreases it by 3 W m^{-2}. This is expected since cloudiness peaks during the day over land whereas it peaks in the night over ocean. The systematic changes between ocean and land, as well as improved agreement with observed fluxes brought about by the use of CERES hourly data (within 2 W m^{-2} difference for the land and the ocean), builds confidence in our use of CERES month-hourly cloud data as the baseline (MACR_BL) for our radiation budget estimates.

4.4.1.3. Daily Variations

[43] The next sensitivity case concerns the impact of daily variations on the simulated monthly mean solar radiation budget (not shown). The solar radiation simulated using ISCCP daily mean cloud data showed little difference (1 W m^{-2}) with that using ISCCP monthly mean cloud data. Basically, for simulating monthly mean solar radiation, daily variations in cloudiness and properties had very little influences on monthly averages. In summary the use of CERES monthly hourly cloud data yields the most desirable simulations of the observed TOA fluxes.

4.4.2. Annual Mean Simulations

[44] Figures 7a and 7b show zonal mean simulations while Table 3 shows the global annual mean fluxes and aerosol/cloud radiative forcing for different aerosol and cloud data under all-sky (Figure 7a and Table 3a) and clear-sky (Figure 7b and Table 3b) conditions. Basically Figure 7 and Table 3 summarize the overall findings of our evaluation study.

4.4.2.1. Zonal Means

[45] Focusing first on Figure 7a for clear-sky TOA reflected solar fluxes, present study (see Table 3b for model inputs) simulated the CERES fluxes within 5 W m^{-2} (i.e., within 1%) and without systematic biases, with the following notable exception. Over ocean, between 30 and 60° in both hemispheres, the simulated values are systematically larger (albeit by 5 W m^{-2} or less). We did not explore the sources for this bias, since they are still within the uncertainties in CERES fluxes and within the uncertainties in the satellite derived AODs. The difference between ERBE and CERES are described in section 2.1.

4.4.2.2. Global Means

[46] Table 3a shows the sensitivity of TOA solar flux, atmospheric solar absorption, surface flux, aerosol radiative forcing (at TOA, within atmosphere and at surface) and cloud radiative forcing to various input parameters used in

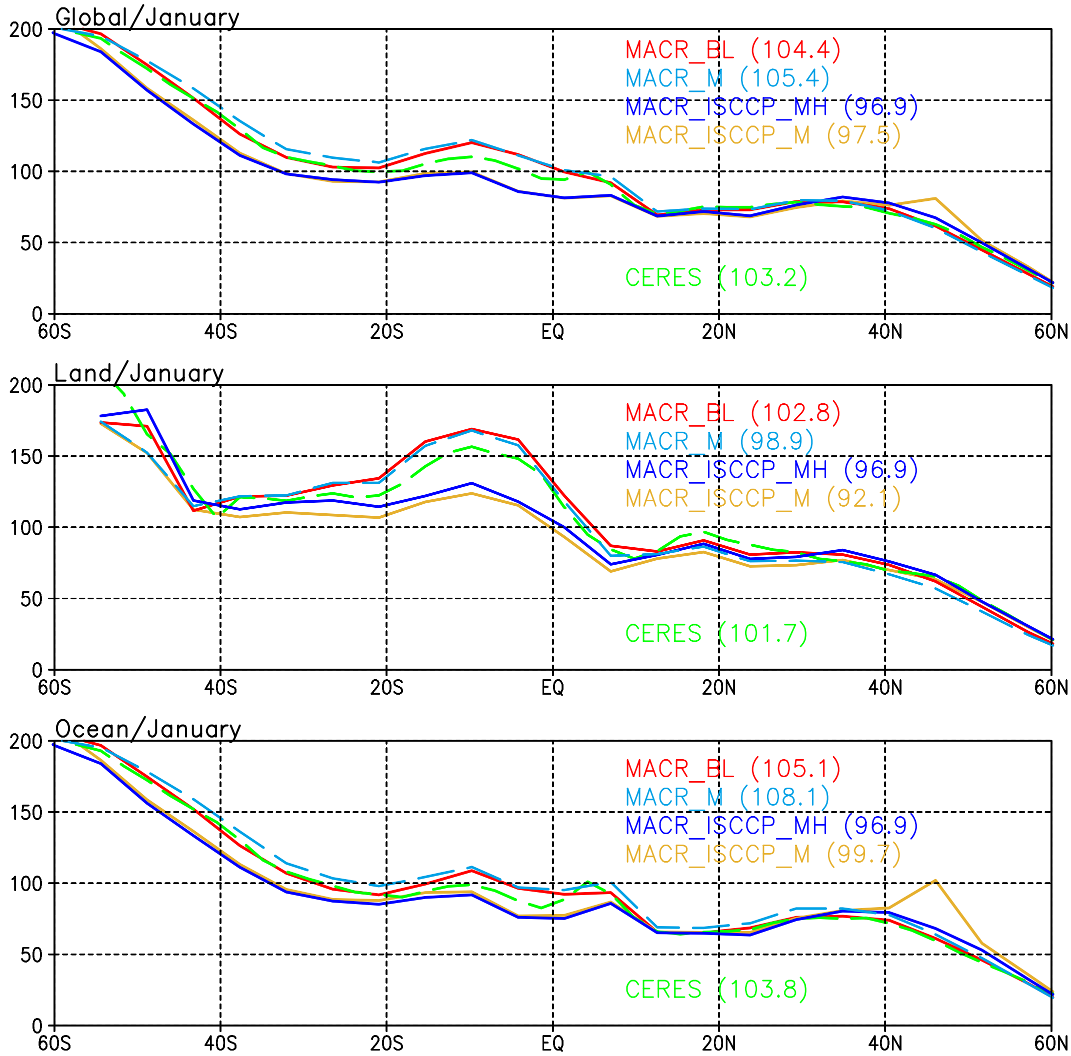

Figure 6. Outgoing TOA fluxes calculated with different cloud data sets over (top) globe, (middle) land, and (bottom) ocean. MACR_BL represents baseline case for MACR calculation, which used MISR monthly mean AODs, and CERES monthly hourly mean clouds (see Table 3). MACR_M is the same as baseline case except for using CERES monthly mean clouds. MACR_ISCCP_MH is the same as baseline case except for using ISCCP monthly 3 hourly clouds. MACR_ISCCP_M is the same as baseline case except for using ISCCP monthly mean clouds. CERES represents CERES observed values. The values in parentheses represent the monthly mean fluxes over globe, land, and ocean.

our simulations. The values shown in Table 3a are for all-sky (clear plus average clouds) conditions. With respect to fluxes (TOA, surface and atmosphere) the sensitivity is about 2% or less. With respect to aerosol radiative forcing, the differences between maximum and minimum values are about 20% for TOA and atmospheric radiative forcing and about 10% for surface forcing. For cloud radiative forcing, the difference between min and max values is about 10%. The differences for clear-sky values (Table 3b) are similar to the values quoted above.

4.5. Summary Assessment of Global Mean Uncertainties

[47] We can objectively estimate the uncertainties in our simulated fluxes only for TOA fluxes, since global annual mean data are available only for TOA fluxes. The uncertainties in CERES fluxes are less than 2 W m^{-2} for global mean monthly flux, while those in ERBE fluxes are 5 W m^{-2} [*Wielicki et al.*, 2006; *Doelling et al.*, 2006; *Barkstrom et al.*, 1989; *Rieland and Raschke*, 1991]. Generally the MACR global mean TOA flux estimates fall within 2 W m^{-2} of CERES value for all cases shown in Figures 7a and 7b, and thus there is neither a need nor a basis to choose one of the many cases as our "best estimate" or "a baseline case." However, on the basis of comparisons shown earlier for station values and monthly mean conditions, we select the model with MISR AOD and CERES month-hourly cloud data as our baseline (i.e., "best estimate") case (see "MACR_BL" in Tables 3 and 4). The uncertainties (2-sigma) around this baseline case are subjectively estimated as follows:

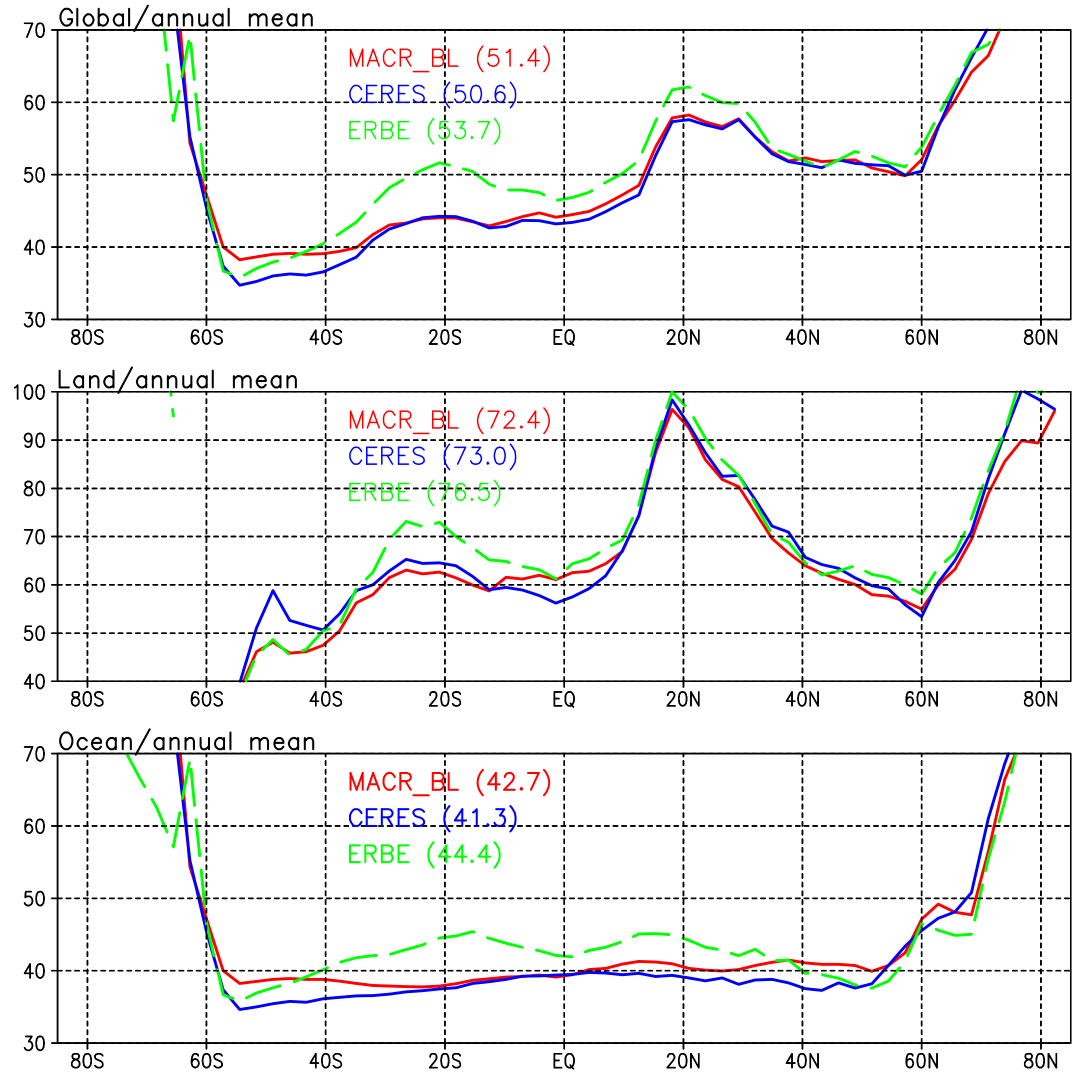

Figure 7a. Comparison of the MACR estimated zonal mean TOA fluxes with CERES and ERBE over (top) the globe, (middle) land, and (bottom) ocean under clear-sky conditions. MACR_BL represents the MACR estimates for baseline case, CERES represents the CERES observations (2000–2002 average), and ERBE represents the ERBE observations (1985–1989 average) in W m^{-2}. The values in parentheses represent the annual mean fluxes over globe, land, and ocean.

[48] For TOA reflected solar flux, we take the difference between maximum and minimum values (rounded off to nearest higher integer value) as our 2-sigma uncertainty value. This procedure yields 4 W m^{-2} for TOA all-sky flux and 2 W m^{-2} for clear-sky flux; and 3 W m^{-2} for TOA cloud forcing. For atmospheric solar absorption under all-sky conditions, the maximum minus minimum from Table 3 is only 1 W m^{-2}. However, we do not think this reflects the true uncertainty in the all-sky absorption. For example, Figure 3 shows a bias of 3 W m^{-2} between the simulated and observed direct solar flux. One interpretation of this bias is that it is solely due to errors in clear-sky solar absorption. Comparison of surface all-sky fluxes with GEBA data reveals a bias of 3.6 W m^{-2} (Figure 5). Again, most of this bias can be due to comparable bias in absorption. We have also ignored internal mixing of aerosols with cloud drops, and the 3-D cloud effect between cloud elements [e.g., *Vogelmann et al.*, 2001]. We recommend using an uncertainty estimate of 5 W m^{-2} for all-sky solar absorption. For clear-sky solar absorption, Table 3a indicates a value of 1 W m^{-2} but we adopt a conservative estimate of 3 W m^{-2} based on the bias in direct solar fluxes (Figure 3). The uncertainties in surface values (fluxes and forcing) are the RMS of the errors in TOA and atmospheric fluxes (assuming uncorrelated errors). For the aerosol radiative forcing terms, instead of quoting mean values and uncertainties, we show the ranges.

5. Solar Radiation Budget, Aerosol, and Cloud Radiative Forcing

[49] The MACR model was run using the 3-year monthly mean inputs for the period from 2000 to 2002. The results

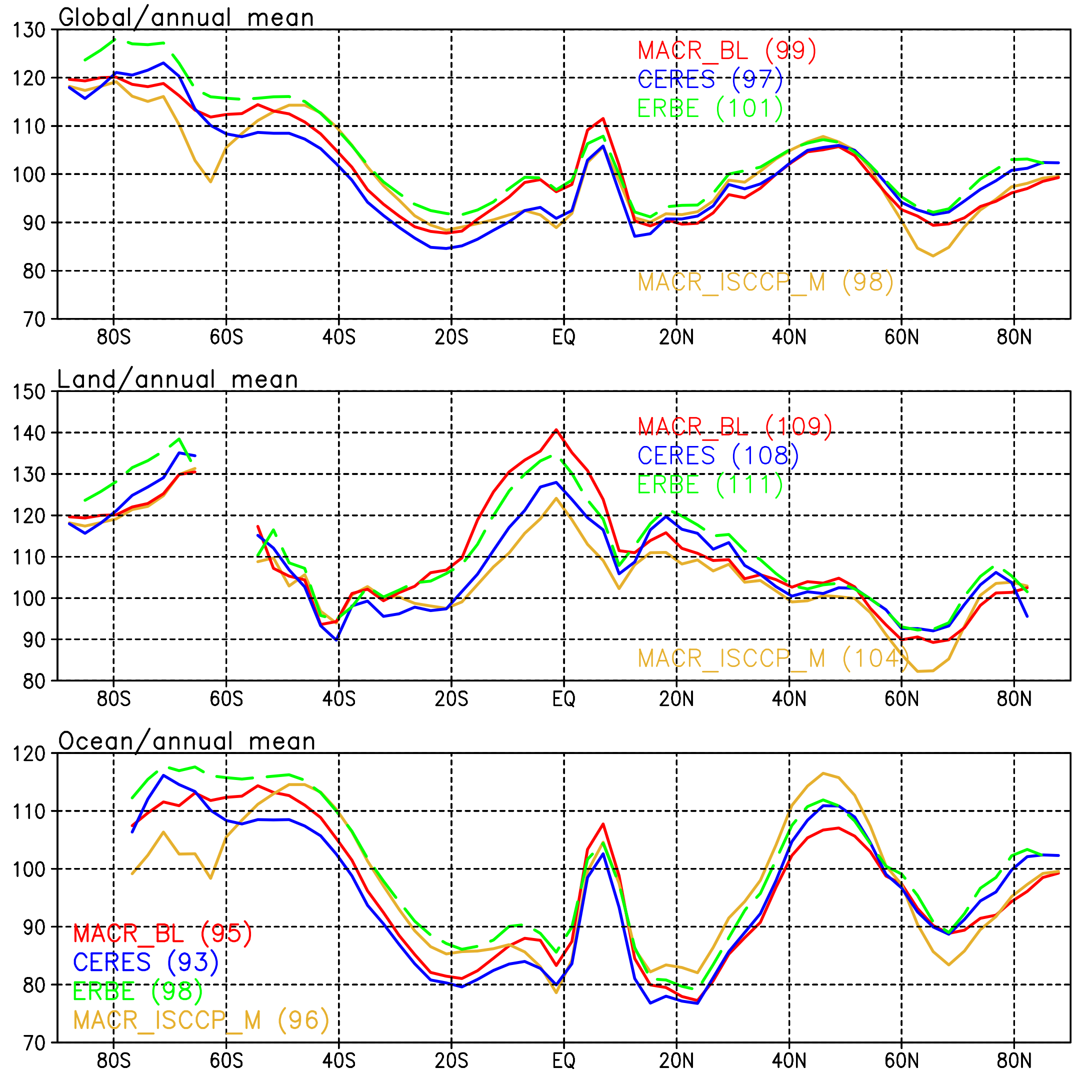

Figure 7b. Same as Figure 7a except under all-sky conditions. MACR_ISCCP_M represents ISCCP monthly mean cloud data are used for MACR calculations. Unit is given in W m^{-2}.

were compared with GEBA observations and with CERES measurements (2000–2002 average).

5.1. Global Average Solar Radiation Budget

[50] The global average solar radiation budget terms are summarized schematically in Figure 8 and compared with published values in Table 4. At the TOA, the net (down minus up) solar flux is 290.4 ± 2 W m^{-2} for clear skies and the presence of clouds reduces it to 242.9 ± 4 W m^{-2}, thus yielding a cloud radiative forcing of −47.5 ± 4 W m^{-2} to be compared with the CERES and ERBE values of −46.5 and −48 W m^{-2} respectively. Thus at the TOA, our simulated values are within a few W m^{-2} of observed values. We note from Table 4 the difference in the reflected solar flux between CERES and ERBE. According to ERBE observations, the reflected solar flux was 101.3 yielding an albedo of 29.6%, whereas CERES value is about 3 ∼ 4 lower at 97.1 ∼ 97.9 yielding an albedo of 28.5 ± 0.1%. Table 4a also reveals that several of the published estimates report global mean albedo larger than the ERBE and the CERES values, with reflected solar fluxes that are larger than CERES values by as much as 8 to 10 W m^{-2}. Similar conclusions are also applicable to clear-sky budget shown in Table 4b.

[51] The atmospheric solar absorption is 72.1 ± 3 W m^{-2} for clear skies and clouds enhance it to 79.3 ± 5 W m^{-2}. The all-sky solar absorption is much larger than the 67 W m^{-2} which are typical of pre-2000 values (e.g., see value of *Intergovernmental Panel on Climate Change* (*IPCC*) [2001] reported in Table 4; *Kiehl and Trenberth* [1997]). It is also larger than the values given in several recent publications (see Table 4 for some examples). Since our simulations agree with TOA as well as the surface solar radiation budget within instrumental errors and within a few W m^{-2} of observed values, we suggest that the current value of solar absorption be treated as an improved estimate. For clear sky, the difference of atmospheric absorption between *IPCC* [2001] and the present study is 12 W m^{-2}, and the same difference exists for cloudy skies. It is assumed that the large difference (12 W m^{-2}) is due to the differences in

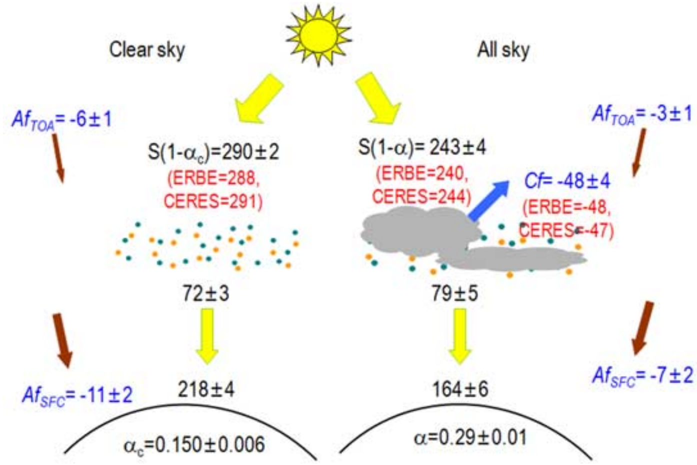

Figure 8. Global annual mean radiative fluxes for clear- and all-sky. S is the solar insolation, α is the planetary albedo, and Af and Cf are the aerosol and cloud radiative forcing. The subscript c denotes clear-sky condition, and TOA and SFC denote TOA and surface, respectively. Present study uses solar constant of 1367 W m^{-2} yielding a global annual mean insolation of 341.8 W m^{-2}. CERES and ERBE use solar constant of 1365 W m^{-2} yielding a global annual mean insolation of 341.3 W m^{-2}. All values are rounded off from Table 4. The units are W m^{-2}.

atmospheric (gases and aerosols) solar absorption. The fundamental reasons for the larger solar absorption in the present study are (1) improved treatment of aerosol absorption, backed by AERONET observations and aerosol chemical models (GOCART). For clear sky, the global aerosol absorption ranges from 4 to 5 W m^{-2} in Table 3b. Aerosol absorption is not considered in pre-2000 model studies [e.g., see *Kiehl and Trenberth*, 1997, Table 4]. (2) Updated spectroscopic parameters for water vapor absorption. The HITRAN 2000 data set [*Rothman et al.*, 2003] provides updated information on several water vapor absorption lines in the near infrared and increases atmospheric absorption by 3 to 4 W m^{-2} when compared with pre-HITRAN 2000 data set [*Bennartz and Lohmann*, 2001; *Albert et al.*, 2004]. In addition, the estimates for absorption by water vapor continuum showed 1 $\sim$ 2 W m^{-2} [*Vogelmann et al.*, 1998; *Fu et al.*, 1998]. These results suggest that the use of updated spectroscopic parameters and continuum absorption for water vapor can increase the atmospheric absorption by up to 4 $\sim$ 6 W m^{-2}, when compared with the pre-2000 model calculations. For clear skies, the present study shows that water vapor accounts for about 50 W m^{-2} of the total atmospheric absorption which is larger than the contribution of water vapor given by *IPCC* [2001] of 43 W m^{-2}. This difference (7 W m^{-2}) of water vapor contribution to total atmospheric absorption is close to the increased atmospheric absorption (4 $\sim$ 6 W m^{-2}) estimated by the updated spectroscopic parameters for water vapor. If we combine aerosol absorption (4 $\sim$ 5 W m^{-2}) with increased atmospheric absorption by updated treatment of water vapor (4 $\sim$ 6 W m^{-2}), the increased atmospheric absorption ranges from 8 to 11 W m^{-2} which is comparable to the difference of total atmospheric absorption (12 W m^{-2}) between *IPCC* [2001] and the present study mentioned above. However, further research is still needed in reducing the uncertainty in our understanding of global average solar absorption, particularly in cloudy skies.

[52] The aerosol radiative forcing is discussed next. At TOA, aerosols enhance the clear-sky reflection by 6 W m^{-2}; that is, TOA aerosol forcing is -5.9 ± 1 W m^{-2} which drops to -3.0 ± 1 W m^{-2} in the presence of clouds (Figure 8). At the surface, the magnitudes of the dimming, 10.7 $\pm$ 2 W m^{-2} for clear skies and 7.4 $\pm$ 2 W m^{-2} for all skies, are larger than the TOA forcing because of atmospheric solar absorption. In other words, both reflection at TOA and atmospheric absorption by aerosols reduce the solar fluxes at the surface. The aerosol forcing includes both natural (e.g., sea salt, sulfates and dust) which are mostly nonabsorbing, and anthropogenic components that include absorbing aerosols such as soot and organics. Aerosol radiative forcing uncertainties were assumed to be random, although there could be systematic biases. The uncertainties in Table 2 were analyzed in an RMS error sense, and overall random uncertainties are 9.0% at TOA and 6.5% at the surface.

[53] The estimated clear-sky TOA forcing was compared with results from similar studies. Table 5 shows the annual mean clear-sky ARF at TOA and the surface over global oceans derived with different methods and data. The MACR estimated forcing over the ocean of about $-5.6 \sim -6.0$ W m^{-2} ($-5.9 \sim -6.2$ W m^{-2} over 60°S $\sim$ 60°N) was a little smaller than the estimated forcing of around -6.4 W m^{-2} (60°S $\sim$ 60°N) from the MODIS by *Bellouin et al.* [2005]. Most of the studies shown in Table 5 agree with the forcing values retrieved by the present study.

[54] It should be noted that the measurement-based estimates of ARF are 30–50% larger than the model-based estimates [*Yu et al.*, 2006]. The global annual mean ARFs for clear sky from AEROCOM (http://nansen.ipsl.jussieu.fr/AEROCOM/) are -3.3 W m^{-2} at TOA and -5.0 W m^{-2} at the surface, respectively, which are 50% smaller than the ARFs at both TOA and the surface in this study (Figure 8). This difference can be caused by overestimated AOD of satellite-based measurement by 10–15% [*Yu et al.*, 2006; *Kinne et al.*, 2006] because of the possible contamination by

Table 5. Annual Mean Clear-Sky Aerosol Radiative Forcing at TOA and the Surface Over Global Ocean Derived With Different Methods and Data

Case	TOA	Surface	Period/Region	Sources
MACR_BL	−6.0 ± 1.0	−9.7 ± 1.5	2000–2002	present study: MACR simulations from MISR AOD
MODIS	−5.6 ± 1.0	−9.0 ± 1.5	2000–2002	present study: MACR simulations from MODIS AOD
MISR+AERONET	−5.0 ± 0.8	−8.2 ± 1.3	2000–2002	present study: MACR simulations from MISR+AERONET AOD
MODIS_A	−5.9	-	2001–2002	*Remer and Kaufman* [2006]
MODIS_B	−6.4	−8.9	2002 (60°S∼60°N)	*Bellouin et al.* [2005]; the latitudinal mean between 60°S and 60°N for the present study ranges from −5.3 to −6.2.
CERES_A	−3.8 ∼ −5.5	-	2000–2001	*Loeb and Manalo-Smith* [2005]
CERES_B	−3.6 ∼ −5.6	-	2000–2003 (35°S∼35°N)	*Loeb and Kato* [2002]; the latitudinal mean between 35°S and 35°N for the present study ranges from −5.5 to −6.0.
MODIS_CERES	−5.3 ± 1.7	-	2000–2001	*Christopher and Zhang* [2004], *Zhang et al.* [2005a, 2005b]
MODIS_GO	−4.5	−9.9	2000–2001	*Yu et al.* [2004]: MODIS+ GOCART AOD
POLDER	−5.0 ∼ −6.0	-	1996–1997	*Boucher and Tanre* [2000]
SeaWiFS	−5.4	−5.9	1997–1998	*Chou et al.* [2002]

thin clouds [*Kaufman et al.*, 2005b; *Remer and Kaufman*, 2006].

5.2. Regional Aerosol Forcing

[55] Figure 9 presents the annual mean aerosol radiative forcing estimated by MACR under clear skies (Figure 9a) and with clouds Figure 9b. In general, the TOA forcing is negative, but areas where the surface albedo is high, such as over ice fields or desert, showed a positive or small negative forcing. The largest atmospheric and negative surface forcings were found over eastern China, India, Mexico, and equatorial Africa. The clear-sky aerosol forcing in Figure 9a and the all-sky forcing in Figure 9b have similar patterns, although the magnitude of the forcing differs somewhat. In Figure 9b the subtropical oceans off East Africa has small negative or positive TOA forcing, which differs from the clear-sky forcing in Figure 9a, because of the presence of low clouds in conjunction with highly absorbing (low SSA) aerosols over this region. Previous studies [e.g., *Podgorny and Ramanathan*, 2001; *Li and Trishchenko*, 2001; *Chung et al.*, 2005] showed that for relatively low SSAs the sign of the TOA forcing can switch from negative when aerosol is below the clouds to positive when aerosol is above the clouds. The large positive forcing over the Polar Regions might be due to the overestimation of MISR AOD values (see Appendix A) as well as high surface albedo.

[56] The regional clear-sky TOA forcings over ocean are compared with the forcing derived by *Yu et al.* [2006]. In general, the annual regional average TOA forcings estimated by MACR_BL are within the observed TOA forcing ranges presented by *Yu et al.* [2006]. For example, the MACR forcing around −8.8 ± 1.8 W m^{-2} over the northwest Pacific (90–180°E, 30–60°N) are in good agreement with the forcing of −9.3 ± 1.5 W m^{-2} by *Yu et al.* [2006]. For tropical Atlantic (0–90°W, 0–30°N) which is influenced by dust from North Africa, the MACR forcing of −8.6 ± 2.6 W m^{-2} should be compared with Yu et al.'s forcing of −8.4 ± 1.3 W m^{-2}. However, for the Arabian Sea and the northern Indian Ocean (0–90°E, 0–30°N), the estimated forcing of −10.5 ± 3.2 W m^{-2} is smaller than Yu et al.'s forcing of −8.4 ± 1.7 W m^{-2}.

5.3. Zonal Mean Cloud Forcing

[57] The latitudinal variations and interhemispheric asymmetries in the simulated cloud forcing (MISR-CERES in Figure 10a) are similar to those revealed in the CERES results. The equatorial minima (i.e., large negative values) in the forcing and the subtropical maxima are respectively due to the presence of the ITCZ cloud systems in the equatorial regions and the low cloudiness associated with the sinking branches of the Hadley cell. Maximum negative cloud forcing ranging from −70 to −80 W m^{-2} is found in the extra tropical storm track cloud systems (45 to 60° in both hemispheres). MACR is able to account for these variations. The differences as large as 10 W m^{-2} exist in the equator to 20°S over land between MACR and observations (CERES and ERBE) with MACR overestimating the reflection of solar radiation by clouds: however, MACR is in better agreement with observed cloud forcing in other latitudes. Cloud forcing with ISCCP clouds is −47.2 W m^{-2} which is within 1 W m^{-2} of the forcing simulated by MACR with CERES (−47.5 W m^{-2}).

[58] Figure 10b shows the annual mean cloud radiative forcing at the TOA for MACR and CERES, as well as the difference between MACR and CERES. The global distributions of cloud radiative forcing of MACR and CERES show similar patterns, despite differences in magnitude of cloud forcing. In general, smaller MACR negative cloud forcings than CERES (positive values in Figure 10b) were found over China, west coast of northern America, and subtropical Pacific Ocean in both hemispheres (around 30–60°), while larger MACR negative cloud forcings (negative values in Figure 10b) were found over the south America and subtropical and equatorial Indian Ocean region in Figure 10b (bottom).These regional differences were also shown by zonal mean cloud forcing in Figure 10a. The monthly mean MACR-CERES cloud forcing differences (not shown) showed almost same patterns as presented in Figure 10b (bottom). Latitudinal differences were less than 5 W m^{-2} for all months except the ITCZ (Intertropical Convergence Zone) and polar region (>60°N) where the MACR-CERES difference is −10 W m^{-2}. Besides, the monthly global mean MACR-CERES cloud forcing differences were less than 3 W m^{-2}, although locally the cloud forcing differences were as large as 15 W m^{-2}. The absolute differences between MACR and CERES over the regions discussed in Figure 10b are larger than 15 W m^{-2}, which is slightly beyond the CERES uncertainty. To investigate this discrepancy, we compared MACR_BL (CERES GEO cloud product in Table 1) simulations with those simulations

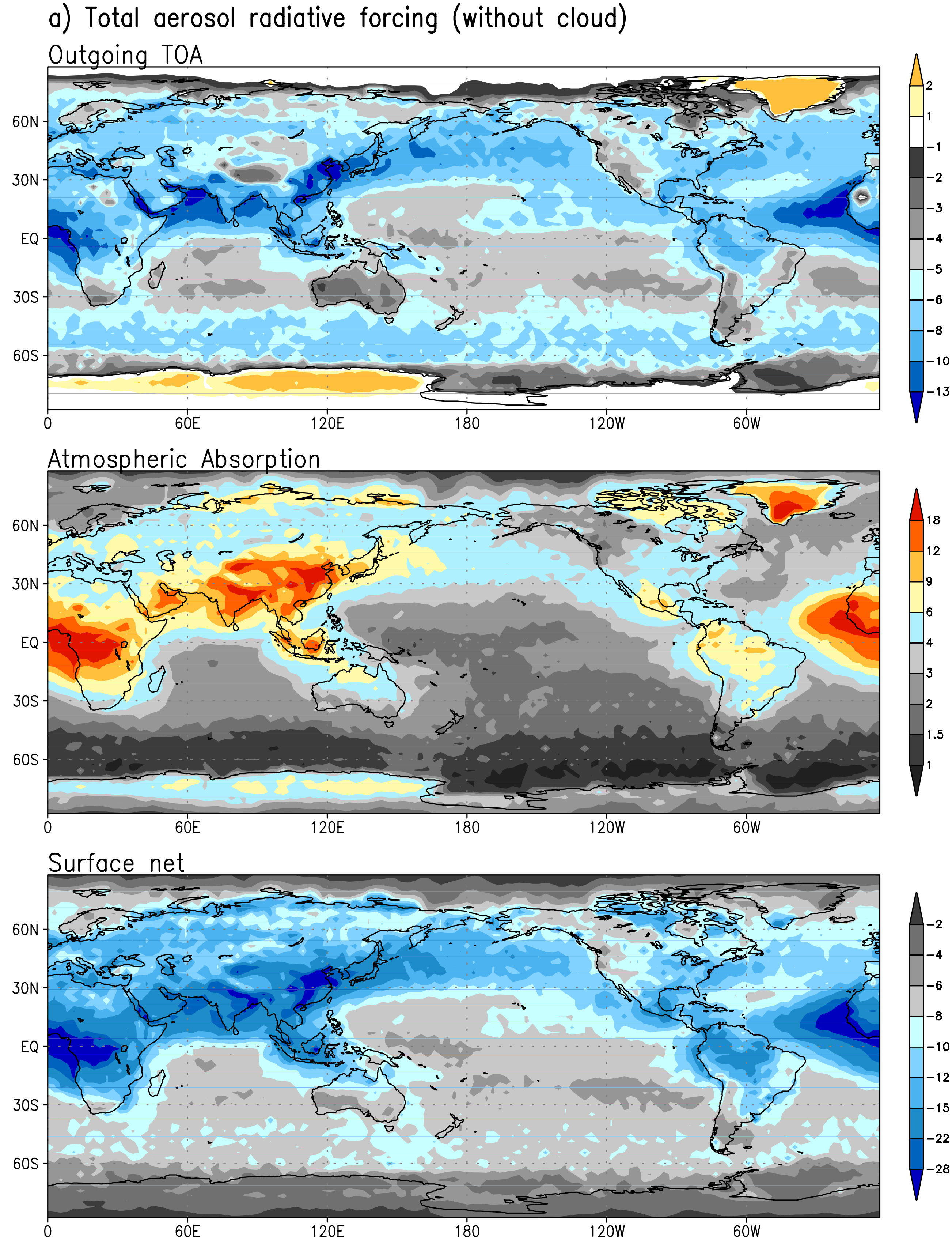

Figure 9a. (top) Annual mean clear-sky aerosol radiative forcing at the TOA, (middle) vertically integrated forcing in the atmosphere, and (bottom) forcing at the surface. The forcing is calculated without cloud effects (clear-sky forcing) given in W m^{-2}.

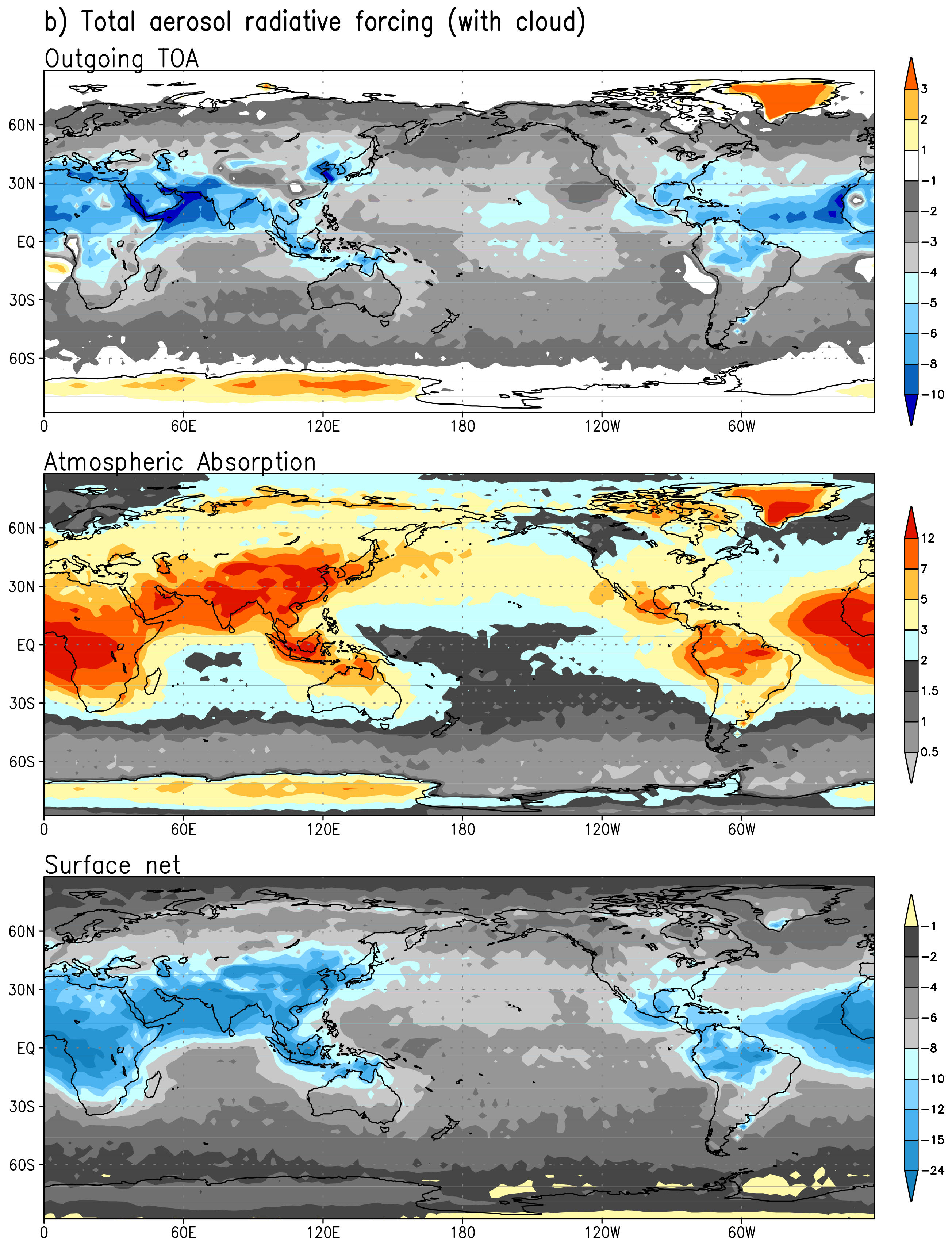

Figure 9b. Same as Figure 9a except aerosol radiative forcing with cloud effect (all-sky forcing).

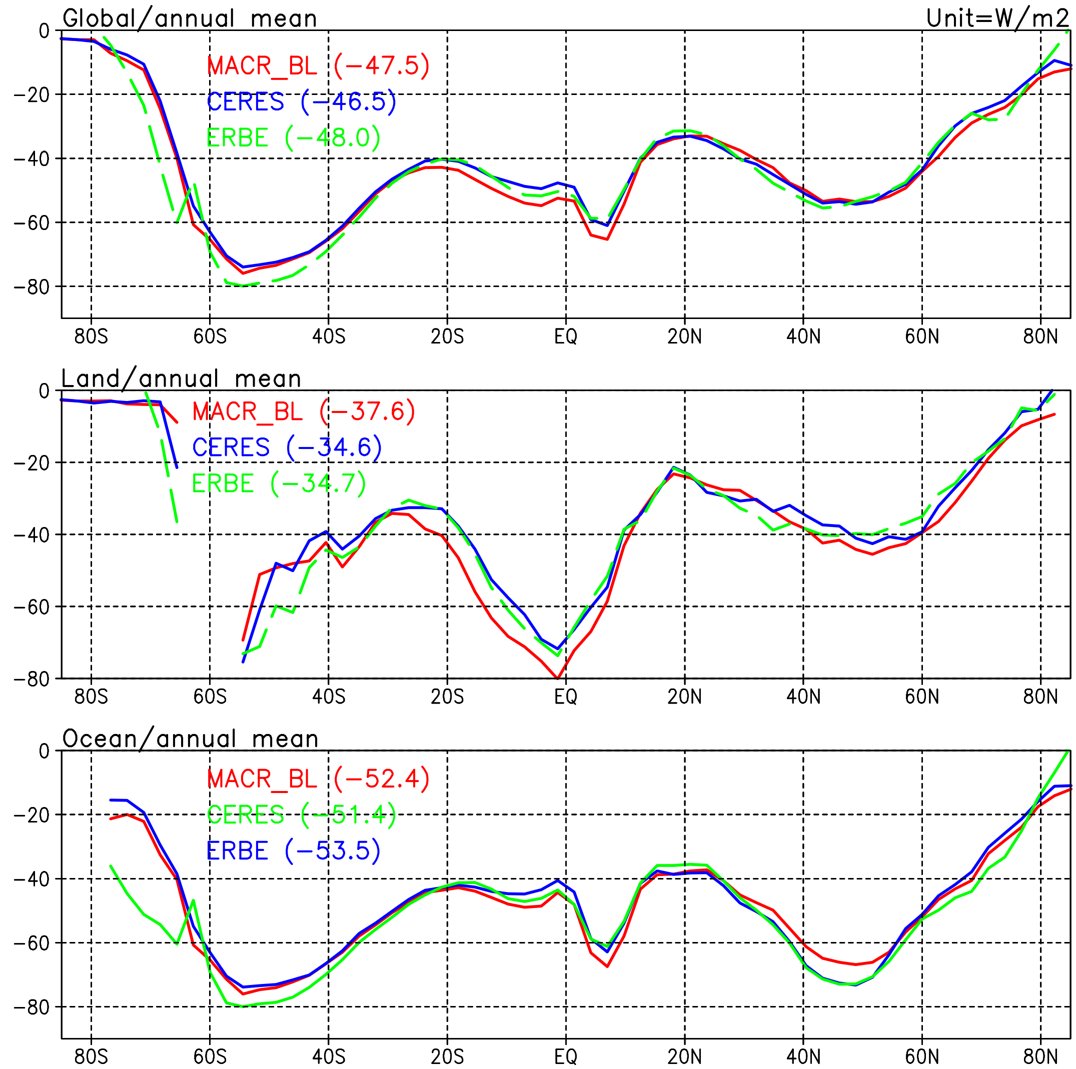

Figure 10a. Comparison of the zonal mean MACR estimated cloud radiative forcing with CERES at the TOA over (top) the globe, (middle) land, and (bottom) ocean. MACR_BL represents the MACR estimates for baseline case, CERES represents the CERES observations (2000–2002 average), and ERBE represents the ERBE observations (1985–1989 average) in W m^{-2}. The values in parentheses represent the annual mean fluxes over globe, land, and ocean.

carried out using different cloud data sets, i.e., ISCCP (referred as $\mathrm{MACR_{ISCCP}}$) and CERES non-GEO cloud data (referred as $\mathrm{MACR_{non\text{-}GEO}}$). There are regions where the cloud forcing difference between $\mathrm{MACR_{non\text{-}GEO}}$ and CERES are larger than 15 W m^{-2}, however these large discrepancies do not regionally coincide with those shown in Figure 10b. Moreover, the large differences in cloud forcing between MACR_BL and $\mathrm{MACR_{non\text{-}GEO}}$ coincide with the regions where the cloud data sets exhibit significant discrepancy in cloud fraction. The large cloud forcing differences between $\mathrm{MACR_{ISCCP}}$ and CERES are found mostly over the equatorial land and ocean, which also indicates the variability due to different cloud data set. In spite of these regional differences, the global annual mean cloud forcing difference is within 1 W m^{-2} (−47.5 W m^{-2} for MACR_BL, −48.1 W m^{-2} for $\mathrm{MACR_{non\text{-}GEO}}$, −48.3 W m^{-2} $\mathrm{MACR_{ISCCP}}$, respectively). The differences among the cloud input data sets is well known (see Table 1 and Figure 1 in http://eosweb.larc.nasa.gov/PRODOCS/ceres/SRBAVG/Quality_Summaries/srbavg_ed2d/fig1.html for comparison among cloud data sets). This suggests that the regional differences in cloud radiative forcing arise from differences in cloud data sets rather than the cloud treatment method in the model.

6. Summary

[59] This study employs a comprehensive set of surface based and satellite borne instrumental data in MACR to estimate the global and regional solar radiation budget, aerosol radiative forcing and cloud radiative forcing at the surface and at the TOA. In order to understand the error in the simulated radiation budget and radiative forcing, MACR simulations were first compared with surface observations

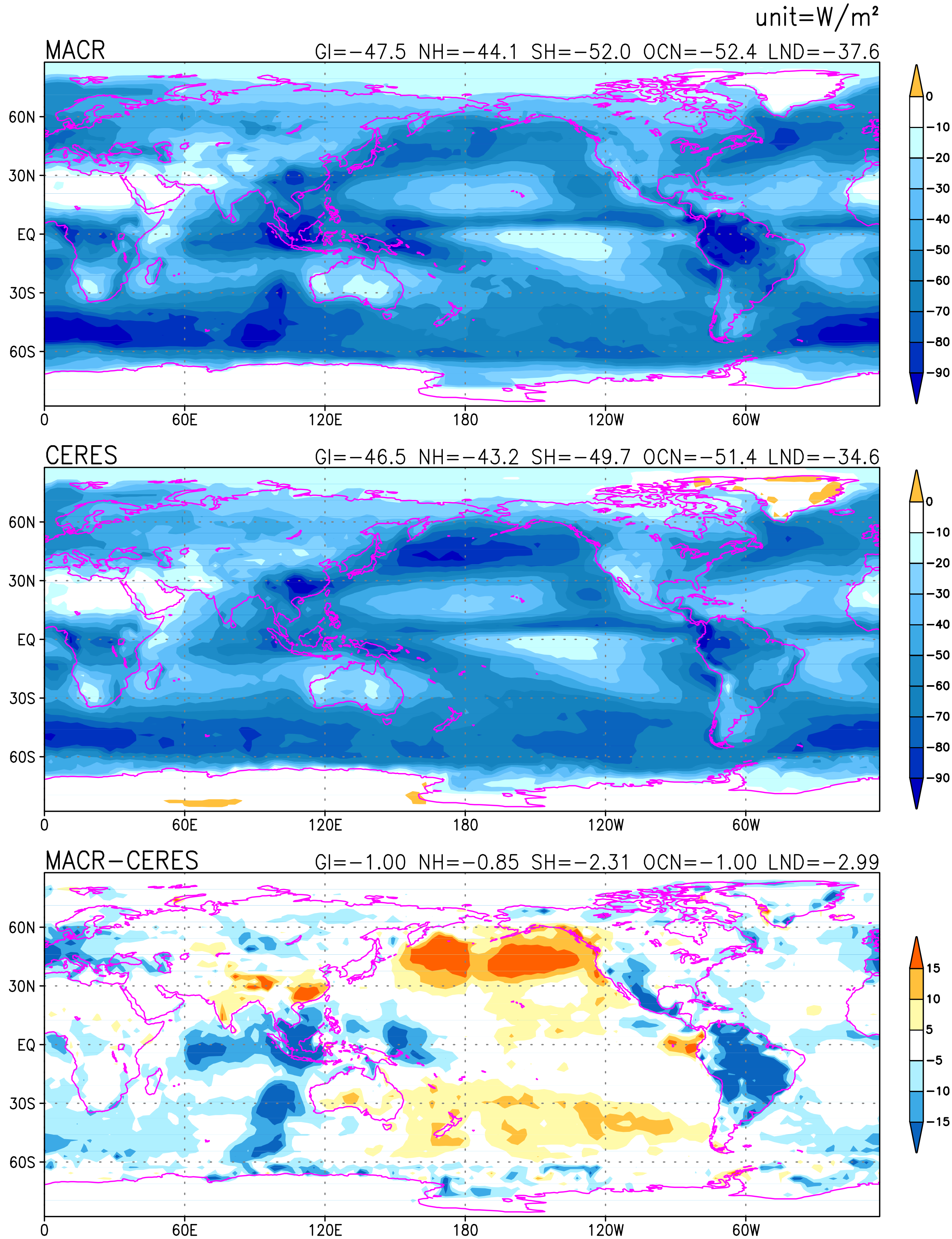

Figure 10b. Annual mean cloud radiative forcing at the TOA for (top) MACR, (middle) CERES, and (bottom) MACR minus CERES given in W m^{-2}. Global (Gl), Northern Hemisphere (NH), Southern Hemisphere (SH), ocean (OCN), and land (LND) averaged values are presented at top right of each panel.

(BSRN and GEBA) and TOA observation (CERES). MACR simulates instantaneous and daily mean surface fluxes within by 4 W m^{-2} under clear-sky conditions. The biases are mostly within the cumulative uncertainties of instruments (5 W m^{-2}). The mean biases for monthly mean surface and TOA fluxes are 3.7 and 1.3 W m^{-2} respectively. The zonal mean MACR values at TOA agree with CERES measurements within 5 $\sim$ 8 W m^{-2} for both clear and all-sky conditions. At TOA, global annual mean MACR fluxes are well within the 3 W m^{-2} uncertainties in CERES fluxes.

[60] Having validated the model with surface and satellite observations and calibrated its uncertainty, we obtained an estimate of the global solar radiation budget, the aerosol radiative forcing and cloud radiative forcing. We estimate the clear-sky albedo to be 15.0 ± 0.6 (%) and the all-sky albedo (average skies) to be 28.9 ± 1.2 (%). MACR retrieved global mean TOA cloud forcing are −47.5 ± 4 W m^{-2}, comparing well with the CERES and ERBE results of −46.5 and −48 W m^{-2}, respectively. However, regionally the cloud forcing differs from CERES by as much as 15 W m^{-2} (20%) differences. The global annual mean atmospheric solar absorption is 72 ± 3 W m^{-2} for clear skies and clouds enhance it to 79 ± 5 W m^{-2}. Clouds decrease the surface solar absorption from 218 ± 4 W m^{-2} to 164 ± 6 W m^{-2}. In general, when compared with MACR, the other model calculations overestimates TOA reflected fluxes by as much as 10% and underestimates atmospheric absorption by 10–20%. In particular, when compared with pre-2000 model studies [e.g., *IPCC*, 2001; *Kiehl and Trenberth*, 1997], MACR global annual average solar absorption is larger by 12 W m^{-2}. This large difference is explained by the updated treatment of aerosols and water vapor absorption. First is the improved treatment of aerosol absorption, backed by AERONET observations and aerosol chemical models (GOCART), which accounts for 4–5 W m^{-2} of the larger solar absorption. Second is the updated treatments for water vapor, i.e., spectroscopic parameters for water vapor absorption by the HITRAN 2000 data set and the inclusion of water vapor continuum, explains 4 $\sim$ 6 W m^{-2} of the additional absorption. Moreover, the trace gases in conjunction with the updated water vapor spectroscopic and water vapor continuum may contribute additional 1 W m^{-2} (diurnal mean) in the atmospheric solar absorption as discussed in Appendix A.

[61] The global mean clear-sky aerosol radiative forcings at TOA and the surface were −5.9 ± 1 and −10.7 ± 2 W m^{-2}, respectively. The presence of clouds changed the TOA forcing from −5.9 ± 1 to −3.0 ± 1 W m^{-2}, and the surface forcing from −10.7 ± 2 to −7.4 ± 2 W m^{-2}. The reduction of the aerosol atmospheric forcing was small from +4.8 ± 1 W m^{-2} without clouds to +4.4 ± 1 W m^{-2} with clouds. For clear-sky aerosol radiative forcing over ocean, MACR forcing agrees with other calculations such as MODIS [*Remer and Kaufman*, 2006; *Bellouin et al.*, 2005; *Yu et al.*, 2004; *Loeb and Manalo-Smith*, 2005; *Loeb and Kato*, 2002], within 0.5 W m^{-2}. Last, MACR is able to reproduce the global mean cloud forcing to within 2 W m^{-2} of the observed values and the zonal forcing to within 5 $\sim$ 10 W m^{-2} and regional forcing to within 15 W m^{-2} values.

[62] In summary, the agreement between simulated and observed values are within experimental errors, for all of the cases considered here: instantaneous fluxes and monthly mean fluxes at stations around the world; TOA fluxes and cloud forcing for global annual mean and zonal mean fluxes; in addition the estimated aerosol forcing at TOA also agrees with other observationally derived estimates. Over all such agreements suggest that global data sets of aerosols and cloud parameters released by recent satellite experiments (MISR; MODIS and CERES) meet the required accuracy to use them as input to simulate the radiative forcing of aerosols and clouds. Last, the atmospheric solar absorption derived in this study should be treated as an improved estimate when compared with earlier published studies.

Appendix A

A1. Comparison Between MISR and MODIS AOD

[63] For aerosol optical depth, both MISR (MISR_AM1_CGAS_F06_0017) and MODIS (MOD08_M3.004) AODs are used for MACR calculation, since the MISR and MODIS used the independent aerosol retrieval strategies and algorithms to exploit the complementary multiangle (MISR) and multispectral (MODIS) nature of their measurements. Figure A1 shows the annual zonal mean AOD comparison between MISR and MODIS for global, land, and ocean during 2000–2002. The MISR global mean AOD is slightly larger than MODIS AOD, and the largest differences are found over high latitude near the polar and northern hemisphere land between 30° and 60°. MODIS AOD over land is larger than MISR AOD by about 0.02 for globe and by 0.05 for 60°S–60°N. On the contrary, MODIS AOD over ocean is smaller than MISR AOD by about 0.02 for globe and by 0.01 for 60°S–60°N, which suggests similar results with *Abdou et al.* [2005]. *Abdou et al.* [2005] showed that over land, MODIS AODs at 660 and 470 nm are larger than those retrieved from MISR by about 10 to 35% on average, while for over ocean, MISR is on average about 0.05 to 0.1 higher than MODIS. These overestimated AODs either over land or over ocean would cause the higher AOD for both MISR and MODIS. Thus the use of MISR or MODIS AODs could derive relatively large ARF at the surface and TOA as discussed in section 5.1. For the MODIS AOD analysis it needs to note that there are missing data over deserts (near 20°N) where MODIS does not retrieve the AOD and filling with zero values, which cause MODIS AOD relative minimum over the region in Figure A1.

[64] Figure A2a shows the comparison of the MACR estimated zonal mean aerosol radiative forcing (ARF) at the TOA over the globe, land, and ocean under clear-sky (Figure A2a) and all-sky (Figure A2b) conditions. For clear sky both MISR and MODIS ARFs show similar patterns with AOD zonal means, while for all-sky ARFs have slightly different patterns with AODs due to the aerosol and cloud interaction. For clear-sky ARFs over high-latitude land show the positive TOA ARF due to bright surface albedo, while negligible positive TOA ARF is found for all-sky because of larger effect of cloud above the aerosol layer than that of surface reflectance. The magnitude of ARF for all-sky is as half as that for clear sky in Figure A2.

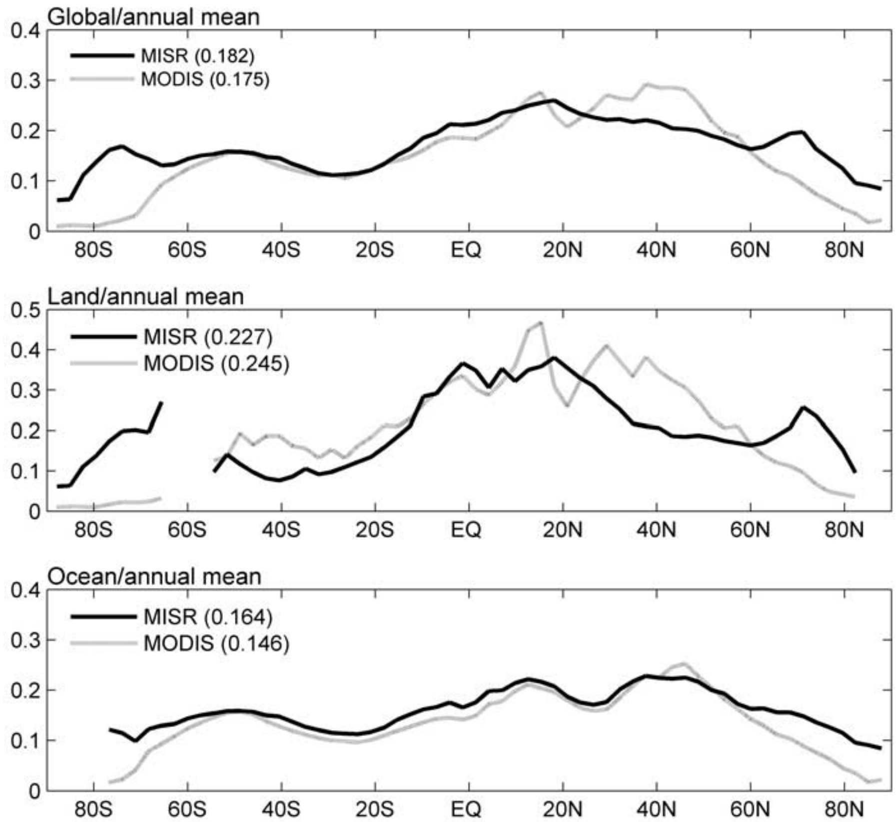

Figure A1. Comparison of annual zonal mean aerosol optical depth between MISR and MODIS over (top) globe, (middle) land, and (bottom) ocean during 2000–2002.

A2. Aerosol Data Integration

[65] Basically, MISR AOD and AERONET aerosol optical properties (AOD, SSA, and asymmetry factor) were used for the model evaluation with the ground-based network (BSRN and GEBA) and satellite based measurements (CERES). For the estimates of global radiation budget, however, the globally distributed aerosol properties were needed. Three different global AODs (MISR, MODIS, and integration of MISR GOCART, and AERONET data) were used for global radiation budget. AOD integration was done with the assumption that the AERONET data were more reliable than MISR retrieved and GOCART simulated data. The data integration method and the detailed description were found in the work of *Chung et al.* [2005]. In this section we briefly summarized the method.

A2.1. Aerosol Optical Depth (AOD)

[66] MISR, AERONET and GOCART climatology products were assimilated statistically. First, the gap of MISR data were filled with GOCART data [*Chin et al.*, 2002] by implementing the iterative difference-successive correction method [*Cressman*, 1959]; that is, we calculated the ratios between MISR and GOCART AODs where there were available MISR AODs, and then used the ratio to correct the GOCART AODs over the neighboring grid points where there were no MISR values. The whole procedure was iteratively repeated, starting from three grid distance away from each MISR AOD point in the first iteration, reducing the distance to one grid at each iteration. Second, AERONET AODs were integrated by employing the technique which used the ratio of mean AERONET AODs to mean MISR + GOCART AODs of their neighboring grids when the AERONET AOD was available at a given grid point in equation (A1). The algorithm used weights with the fourth power of the distance from the location of the grid.

[67] At each grid, say j, with a MISR + GOCART AOD (AOD^{MG}), we let:

$$AOD_j = AOD_j^{MG} \times \frac{\sum_i \frac{AOD^{AER}_{j,i}}{dj,i^4}}{\sum_i \frac{AOD^{MG}_{j,i}}{dj,i^4}} \qquad (A1)$$

where AOD^j is the adjusted new value of the AOD at grid j, $AOD^{AER}_{j,i}$ is an AERONET AOD at station location i nearby the grid j, dj,i is the distance between j and i, $AOD^{MG}_{j,i}$ is the MISR + GOCART AOD at the grid which has the AERONET AOD location i. If there were quite a few AERONET AODs near the grid j, the algorithm weighted them according to the distance from the location of the grid j as in equation (A1).

[68] The integrated AOD from MISR, AERONET and GOCART shows slightly smaller mean AOD around 0.16 over globe, around 0.20 over land, and around 0.14 over ocean compared with MISR and MODIS AOD in Appendix A1.

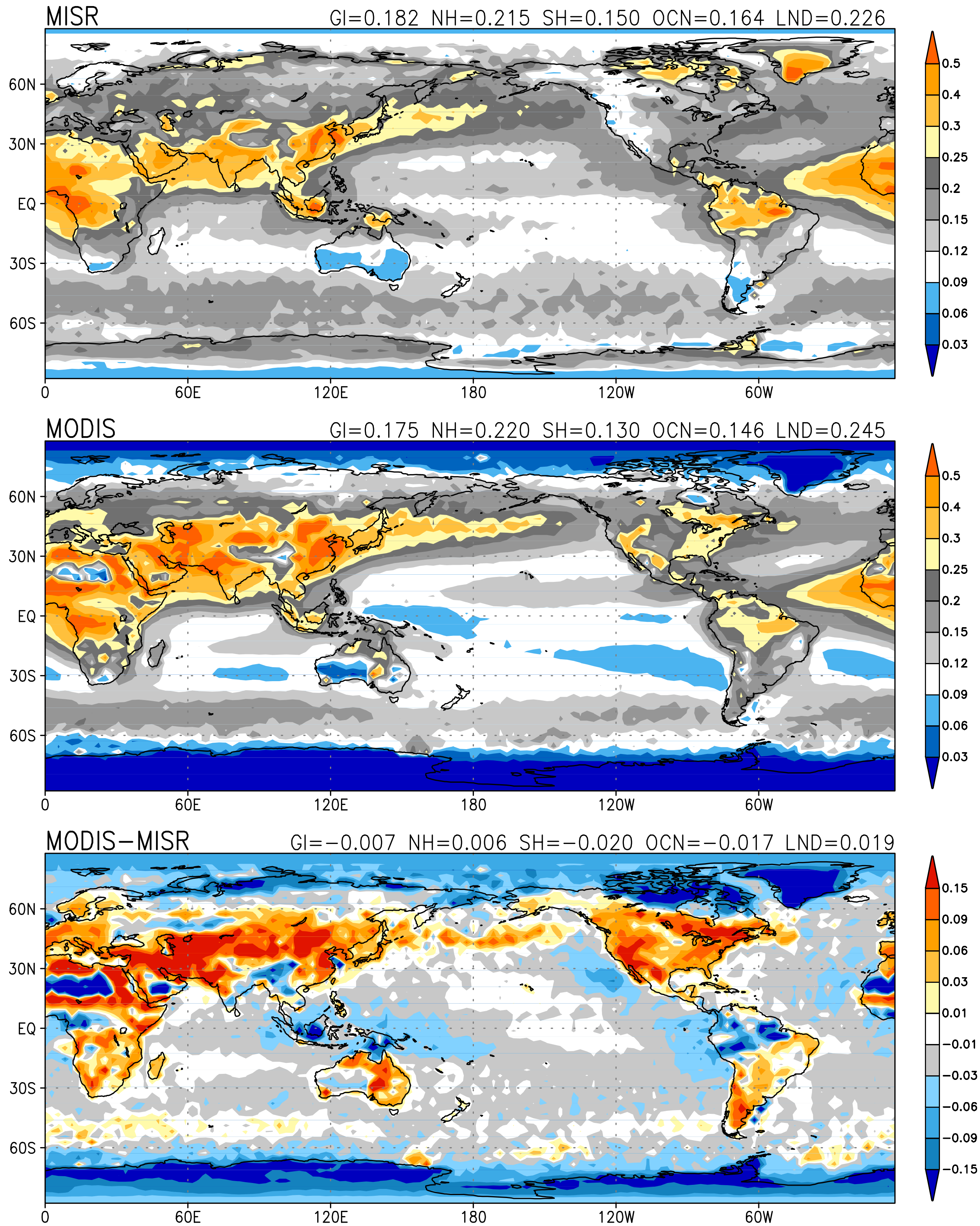

Figure A1b. Annual mean aerosol optical depth for (top) MISR, (middle) MODIS, and (bottom) MODIS minus MIDSR during 2000–2002.

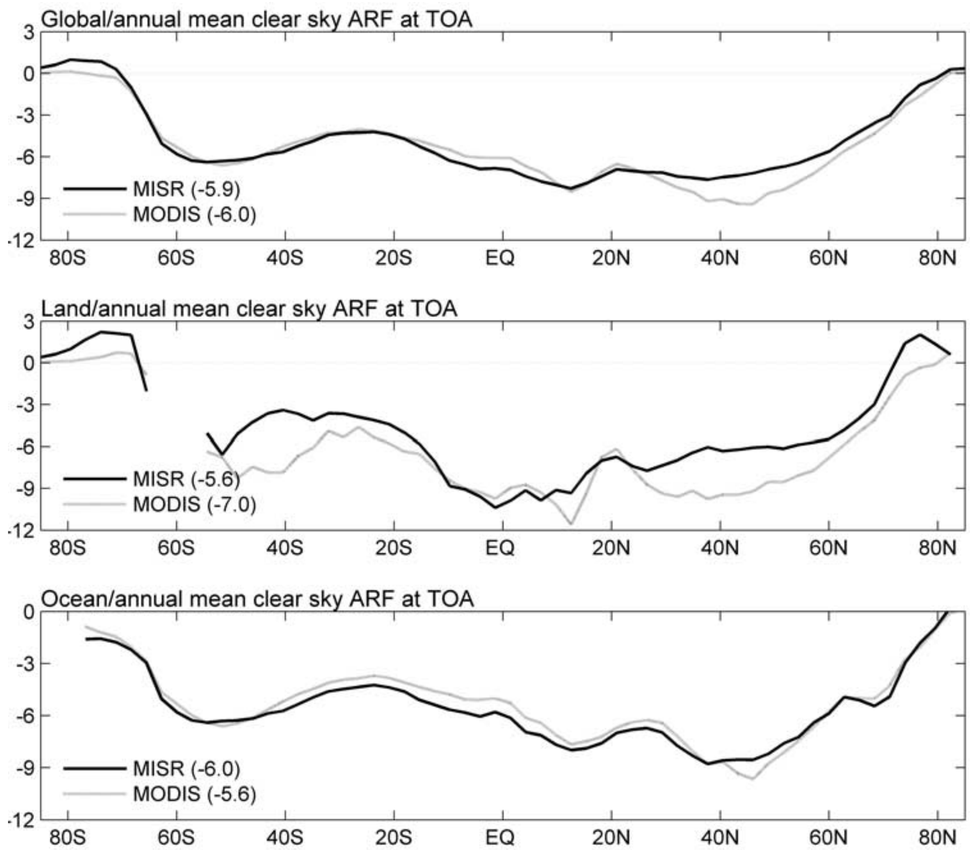

Figure A2a. Comparison of the MACR estimated zonal mean aerosol radiative forcing at the TOA over (top) the globe, (middle) land, and (bottom) ocean under clear-sky conditions. MISR represents the MACR estimates with MISR AOD data, and MODIS represents the MACR estimates with MODIS AOD data in W m^{-2}.

A2.2. Single Scattering Albedo (SSA)

[69] The global SSAs was first derived from GOCART simulations which were derived by weighting the individual SSAs for BC, sulfate, OC, dust and sea salt with their respective AODs. In doing so, we assumed that sulfate, OC and sea salt SSA were 1.0 and the BC SSA was 0.2 [*Satheesh et al.*, 1999; *Hess et al.*, 1998]. The dust SSA was allowed to vary from 0.9 to 0.98 depending on the amount of BC to consider their mixing status. The dust SSA was set to 0.98, when the ratio of BC AOD to BC + dust AOD was less than 0.1, and the dust SSA was 0.9 when the ratio was greater than 0.5. Over China and the northern Pacific, the dust SSA is prescribed differently. The dust_SSA for all of China is assumed to be 0.9 and linearly increases from 0.9 over the northwestern Pacific (off of China) to roughly 0.95 over the northeastern Pacific (off of the west coast of North America). The parameterization described above for dust SSA was motivated by the AERONET results reported by *Eck et al.* [2001, 2005] and the field studies off of Asia reported by *Clarke et al.* [2004] and *Kim et al.* [2005]. These SSAs were subsequently adjusted with the AERONET SSAs. The adjustment procedure is similar to that described for AOD. In Figure A3a (GOCART + AERONET SSA), South Africa, south and east Asia, and Mexico represent relatively high absorbing aerosol regions.

A2.3. Asymmetry Parameter (g)

[70] The global asymmetry parameters were derived similarly to SSAs. The asymmetry parameters of five aerosol types from the Optical Properties of Aerosols and Clouds (OPAC) [*Hess et al.*, 1998] were weighted with the corresponding GOCART AODs, and then, the values were adjusted with the AERONET asymmetry factors. Figure A3b shows the asymmetry parameter (g) derived from GOCART products after it was adjusted with AERONET values.

A2.4. Spectral Dependence (α)

[71] The wavelength dependences of the aerosol parameters were derived using an Angstrom-like representation, defined as follows:

$$X(\lambda) = X(0.55\mu m)\left(\frac{\lambda}{0.55}\right)^{-a} \quad \text{(A2)}$$

where X can be AOD, SSA or the asymmetry factor, and λs are wavelengths given in micrometer. The exponent alphas per aerosol parameter (AOD, SSA, and asymmetry factor) were parameterized by αs and AODs of different aerosol types, i.e., BC, sulfate, OC, dust, and sea salt. We obtained

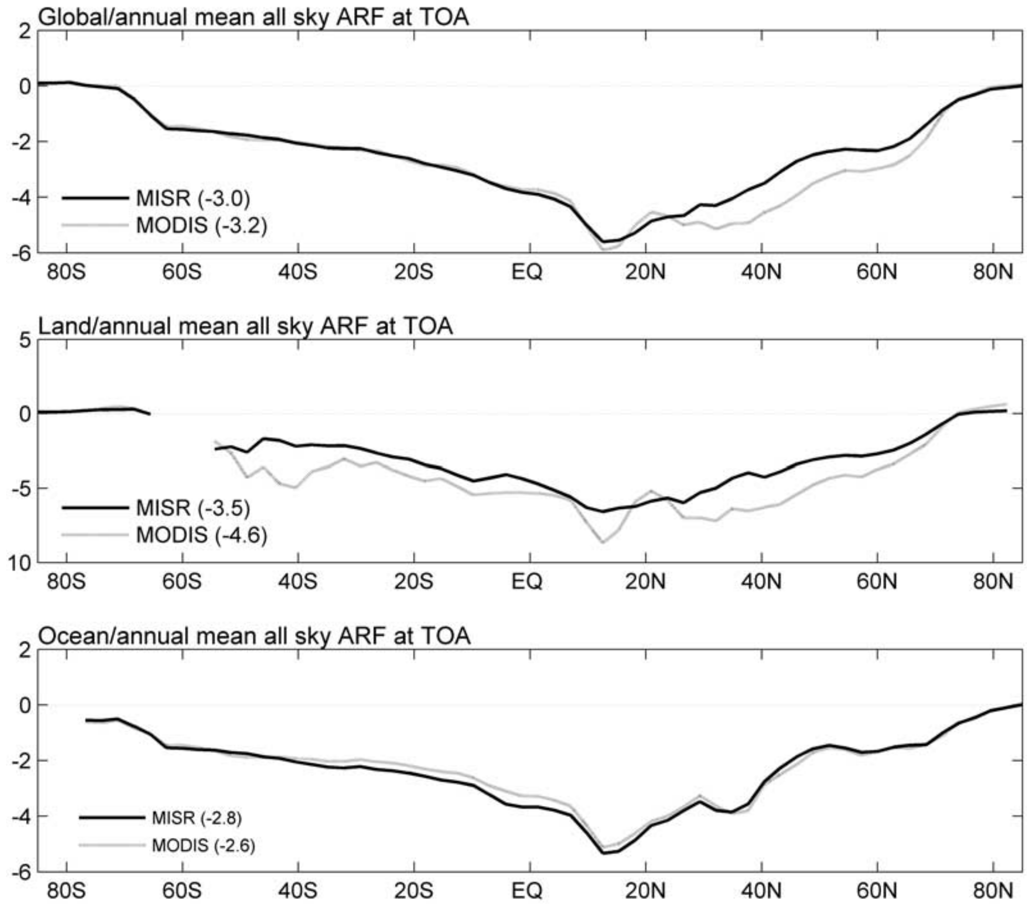

Figure A2b. Same as Figure A2a except under all-sky conditions.

the empirical values of α for different aerosol types from the AERONET results published in the literature [e.g., *Dubovik et al.*, 2002; *Eck et al.*, 2001]. The α of asymmetry factor was derived from relationship between α(AOD) and α(g) with a cubic polynomial.

$$\alpha(AOD) = \frac{1.9 \times AOD_{BC} + 1.7 \times AOD_{OC+sulfate} + 1.4 \times AOD_{seasalt} + 0.6 \times AOD_{dust}}{AOD_{total}} \quad \text{(A3)}$$

$$\alpha(SSA) = \frac{0.078 \times AOD_{BC} + 0.0 \times AOD_{OC+sulfate} + 0.012 \times AOD_{seasalt} - 0.068 \times AOD_{dust}}{AOD_{total}} \quad \text{(A4)}$$

$$\alpha(g) = 0.1288 \times a(AOD)^3 - 0.1983 \times a(AOD)^2 + 0.0618 \times a(AOD) + 0.0502 \quad \text{(A5)}$$

[72] To investigate the uncertainties due to the assumption of wavelength-dependent aerosol optical properties, sensitivity tests were made with Angstrom parameters (α) from different data sets. The first input, α, are retrieved from AERONET data at 270 sites from 1993 to 2003 and used as input to the MACR simulations. Because of the lack of global coverage of AERONET retrieved α, we segregated the data on the basis of regions (continents are North America, South America, Asia, etc; oceans are North Atlantic, South Atlantic, etc) and the regional monthly mean α are given as input to the MACR calculations. For the second input parameters, we integrated AOD, SSA and g to obtain the correct α. We used GOCART as well as AERONET data sets simultaneously, in such way that GOCART values are adjusted with AERONET data. Figure A4 shows the differences in α (AOD and SSA) among these data sets considered in this sensitivity study. On regional level, the annual mean α(AOD) from AERONET is relatively smaller than that of GOCART (see equation (A3)), while α(SSA) from AERONET is larger than that of GOCART (see equation (A4)). These differences among these input data sets may provide us the uncertainty estimates.

[73] The MACR simulations have been carried out using these two input data sets for α and keeping all other input

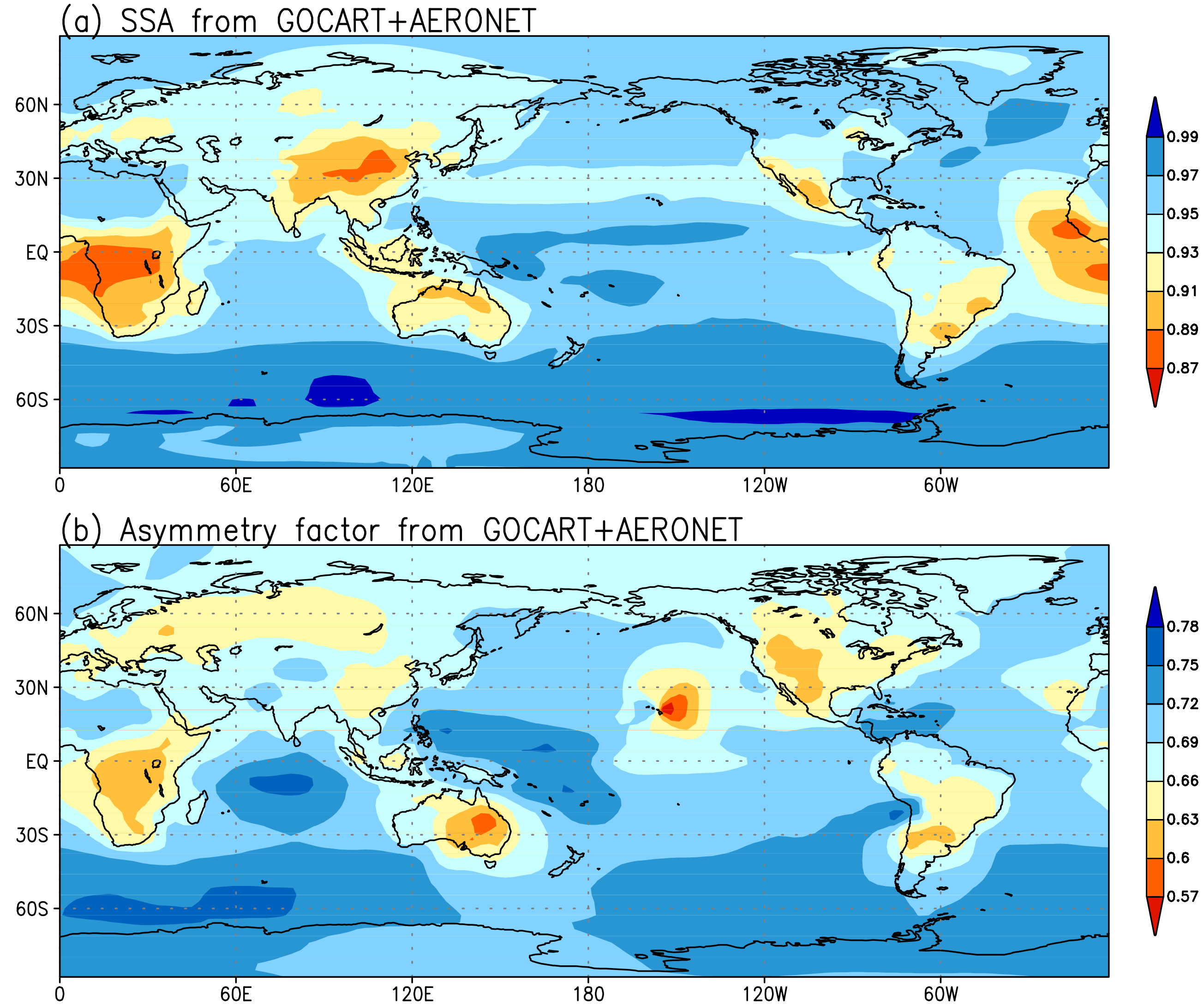

Figure A3. SSA and asymmetry factor (550 nm) derived from GOCART products which are adjusted with AERONET SSAs. SSA and asymmetry factor are for springtime (March to May).

parameters the same under the clear-sky conditions. The calculated MACR fluxes (i.e., AERONET is referred as MACR_α_{AE}; GOCART + AERONET is referred as MACR_α_{GA}) are then compared with baseline MACR calculations (MACR_BL). At TOA, MACR α_{AE} and MACR α_{GA} global annual mean outgoing fluxes are biased by -0.18 and -0.07 W m^{-2}, respectively when compared to MACR BL. At the surface, the net fluxes contain biases of 0.57 and 0.40 W m^{-2}, respectively. These results suggest that the wavelength dependence of aerosol optical properties is not critical to the total global mean aerosol direct radiative forcing for clear sky; but more spatial observational data sets is needed to reduce the uncertainties in the input data and to increase the model accuracies.

A3. Trace Gas Absorption

[74] To estimate the contribution of trace gases to the solar absorption, we used radiative transfer (RT) model developed by the Center for Climate System Research, University of Tokyo, Japan, since the MACR version used in this study incorporates only major gaseous absorption (H_2O, CO_2, O_3, and O_2). The RT model accounts for multiple scattering in the atmosphere by molecules and aerosol particles, and bidirectional surface reflection [*Nakajima and Tanaka*, 1986, 1988]. We carried out RT model simulation using two different gaseous absorption databases: one uses LOWTRAN-7 database [*Kneizys et al.*, 1988], and the other uses HITRAN 2004 database [*Rothman et al.*, 2005].

[75] Figure A5 shows the atmospheric solar absorption in the broadband region by trace gases. Trace gas absorption value obtained using HITRAN database is larger than LOWTRAN database by about 30% consistent at all solar zenith angle. Trace gas absorption in tropics (TRO) is slightly larger than that of high-latitude winter (HLW) by about 0.5 W m^{-2}. Diurnal mean atmospheric absorption ranges from 1.1 to 1.6 with HITRAN database, while 0.8 to 1.2 with LOWTRAN database, which indicates that the updated trace gaseous spectroscopic database increases the

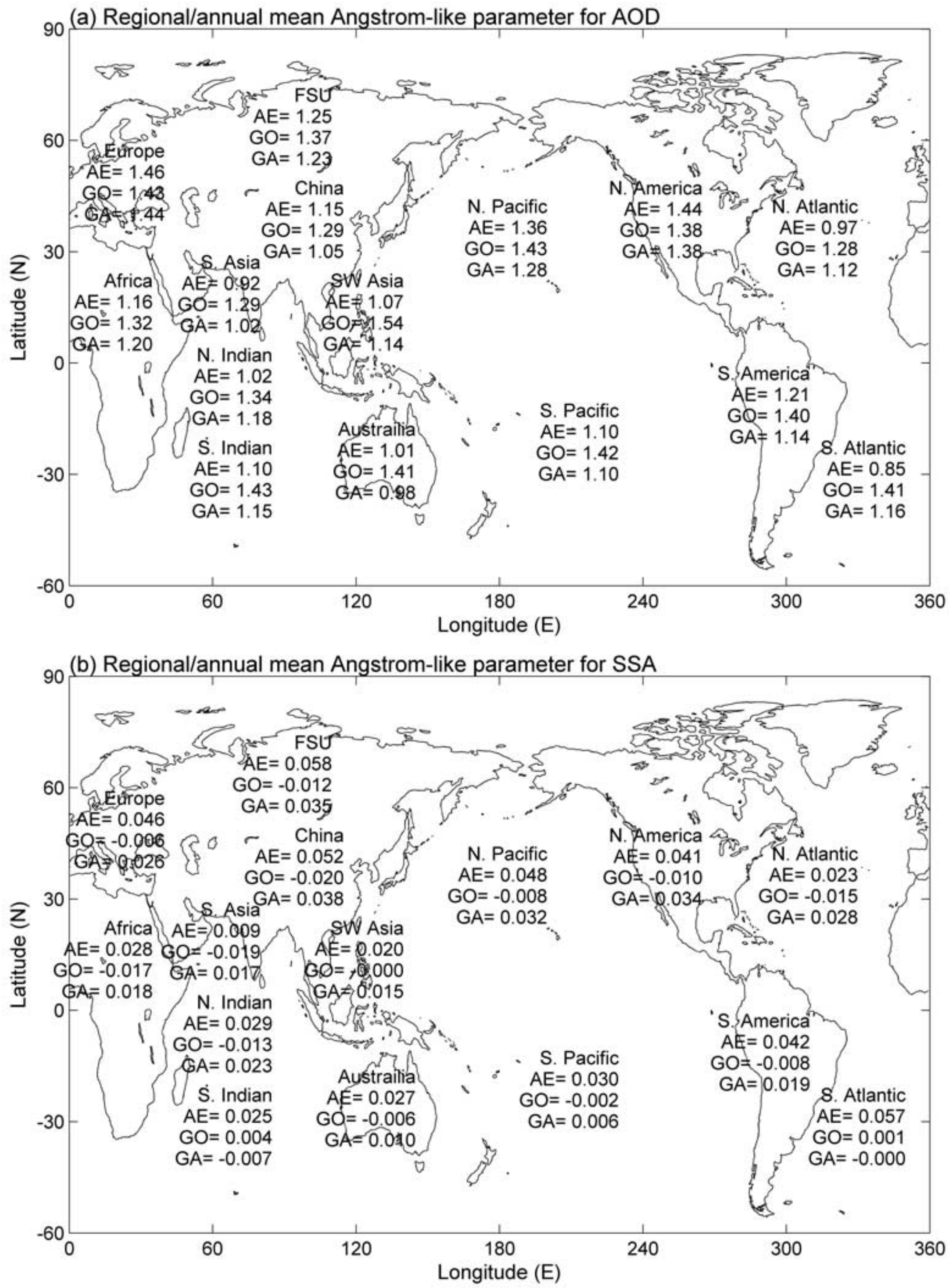

Figure A4. Regional/annual mean Angstrom-like parameters for (a) AOD and (b) SSA with different source of data set for MACR calculations. AE represents the AERONET data set, GO is GOCART which is used for this study (equations (A3)–(A5)), and GA represent the GOCART + AERONET.

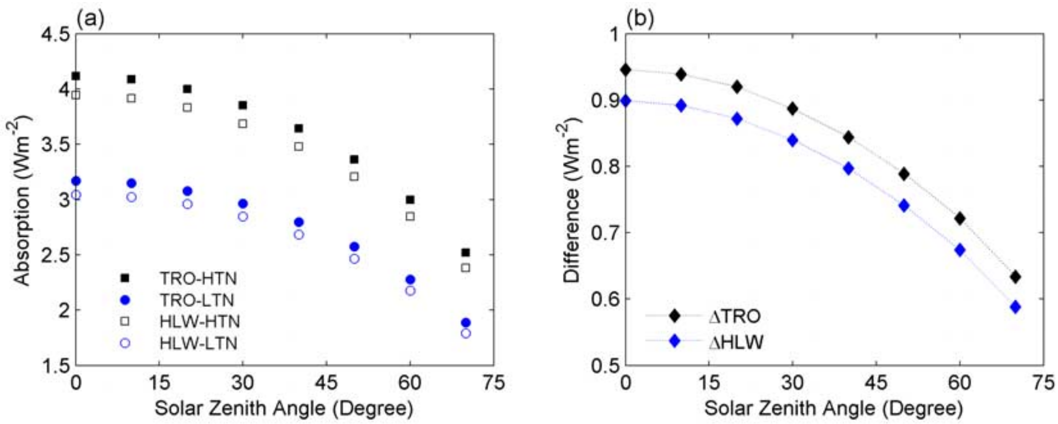

Figure A5. (a) Broadband global solar flux absorption in the atmosphere by the trace gases as function of solar zenith angle for tropical (TRO) and high-latitude winter (HLW) atmosphere obtained from both HITRAN 2004 (HTN) and LOWTRAN 7 (LTN) database and (b) the absorption difference between HITRAN and LOWTRAN.

diurnal mean atmospheric SW absorption by 0.3–0.4 W m^{-2}. These results suggest that the trace gaseous absorption in solar radiative transfer calculations needs to be accounted to improve our understanding of the global solar radiation budget.

[76] **Acknowledgments.** This paper benefited significantly from detailed comments by the anonymous reviewers. We are indebted to them for numerous technical and editorial suggestions which were incorporated in the revised version. We would like to thank A. Ohmura for providing the GEBA data for the evaluation of MACR radiative transfer model. We would also like to thank WCRP/BSRN for providing the BSRN data. MISR, MODIS, NVAP and CERES data were obtained from the Atmospheric Sciences Data Center at NASA Langley Research Center, and AERONET and TOMS data were obtained from the NASA Goddard Space Flight Center. This study was funded by NSF grant (ATM-0201946) and NOAA grant (NA17RJ1231-VR03). We thank B. Wielicki for numerous clarifications on the use of CERES radiation budget data.

References

Abdou, W. A., D. J. Diner, J. V. Martonchik, C. J. Bruegge, R. A. Kahn, B. J. Gaitley, K. A. Crean, L. A. Remer, and B. Holben (2005), Comparison of coincident Multiangle Imaging Spectroradiometer and Moderate Resolution Imaging Spectroradiometer aerosol optical depths over land and ocean scenes containing Aerosol Robotic Network sites, *J. Geophys. Res.*, *110*, D10S07, doi:10.1029/2004JD004693.

Albert, P., K. M. Smith, R. Bennartz, D. A. Newnham, and J. Fischer (2004), Satellite- and ground-based observations of atmospheric water vapor absorption in the 940 nm region, *J. Quant. Spectrosc. Radiat. Transfer*, *84*, 181–193.

Arking, A. (1996), Absorption of solar energy in the atmosphere: Discrepancy between model and observations, *Science*, *273*, 779–782.

Barker, H. W., et al. (2003), Assessing 1D atmospheric solar radiative transfer models: Interpretation and handling of unresolved clouds, *J. Clim.*, *16*, 2676–2699.

Barkstrom, B., E. Harrison, G. Smith, R. Green, J. Kibler, R. Cess, and the ERBE Science Team (1989), Earth Radiation Budget Experiment (ERBE) archival and April 1985 results, *Bull. Am. Meteorol. Soc.*, *70*, 1254–1262.

Bellouin, B., O. Boucher, J. Haywood, and M. S. Reddy (2005), Global estimates of aerosol direct radiative forcing from satellite measurements, *Nature*, *438*, 1138–1140.

Bennartz, R., and U. Lohmann (2001), Impact of improved near infrared water vapor line data on absorption of solar radiation in GCMs, *Geophys. Res. Lett.*, *28*, 4591–4594.

Boucher, O., and D. Tanre (2000), Estimation of the aerosol perturbation to the Earth's radiative budget over oceans using POLDER satellite aerosol retrievals, *Geophys. Res. Lett.*, *27*, 1103–1106.

Briegleb, B., and V. Ramanathan (1982), Spectral and diurnal variations in clear sky planetary albedo, *J. Appl. Meteorol.*, *21*, 1160–1171.

Briegleb, B., P. Minnis, V. Ramanathan, and E. Harrison (1986), Comparison of regional clear-sky albedos inferred from satellite observations and model computations, *J. Clim. Appl. Meteorol.*, *25*, 214–226.

Chen, T., Y. Zhang, and W. B. Rossow (2000), Sensitivity of atmospheric radiative heating Rate profiles to variations of cloud layer overlap, *J. Clim.*, *13*, 2941–2959.

Chin, M., P. Ginoux, S. Kinne, O. Torres, B. N. Holben, B. N. Duncan, R. V. Martin, J. A. Logan, A. Higurashi, and T. Nakajima (2002), Tropospheric aerosol optical thickness from the GOCART model and comparisons with satellite and sunphotometer measurements, *J. Atmos. Sci.*, *59*, 461–483.

Chou, M. D., P. K. Chan, and M. Wang (2002), Aerosol radiative forcing derived from SeaWiFS-retrieved aerosol optical properties, *J. Atmos. Sci.*, *59*, 748–757.

Christopher, S. A., and J. Zhang (2002), Shortwave Aerosol Radiative Forcing from MODIS and CERES observations over the oceans, *Geophys. Res. Lett.*, *29*(18), 1859, doi:10.1029/2002GL014803.

Christopher, S. A., and J. Zhang (2004), Cloud-free shortwave aerosol radiative effect over oceans: Strategies for identifying anthropogenic forcing from Terra satellite measurements, *Geophys. Res. Lett.*, *31*, L18101, doi:10.1029/2004GL020510.

Chu, D. A., Y. J. Kaufman, C. Ichoku, L. A. Remer, D. Tanré, and B. N. Holben (2002), Validation of MODIS aerosol optical depth retrieval over land, *Geophys. Res. Lett.*, *29*(12), 8007, doi:10.1029/2001GL013205.

Chung, C. E., V. Ramanathan, D. Kim, and I. A. Podgorny (2005), Global anthropogenic aerosol direct forcing derived from satellite and ground-based observations, *J. Geophys. Res.*, *110*, D24207, doi:10.1029/2005JD006356.

Clarke, A. D., et al. (2004), Size distributions and mixtures of dust and black carbon aerosol in Asian outflow: Physiochemistry and optical properties, *J. Geophys. Res.*, *109*, D15S09, doi:10.1029/2003JD004378.

Clough, S. A., F. X. Kneizys, and R. W. Davies (1989), Line shape and the water vapor continuum, *Atmos. Res.*, *23*, 229–241.

Collins, W. D., J. K. Hackney, and D. P. Edwards (2002), An updated parameterization for infrared emission and absorption by water vapor in the National Center for Atmospheric Research Community Atmosphere Model, *J. Geophys. Res.*, *107*(D22), 4664, doi:10.1029/2001JD001365.

Conant, W. C. (2000), An observational approach for determining aerosol surface radiative forcing: Results from the first field phase of INDOEX, *J. Geophys. Res.*, *105*, 15,347–15,360.

Cressman, G. P. (1959), An operational objective analysis system, *Mon. Weather Rev.*, *87*, 367–374.

Di Girolamo, L., and M. J. Wilson (2003), A first look at band-differenced angular signatures for cloud detection from MISR, *IEEE Trans. Geosci. Remote Sens.*, *41*, 1730–1734.

Diner, D. J., et al. (1998), Multiangle Imaging Spectroradiometer (MISR) description and experiment overview, *IEEE Trans. Geosci. Remote Sens.*, *36*, 1072–1087.

Doelling, D. R., D. F. Keyes, D. F. Young, B. A. Wielicki, and T. Wong (2006), The newly released 5-year Terra-based monthly CERES radiative flux and cloud product, paper presented at 12th Conference on Atmospheric Radiation, Am. Meteorol. Soc., Madison, Wis., 10–14 July.

Dubovik, O., A. Smirnov, B. N. Holben, M. D. King, Y. J. Kaufman, and I. Slutsker (2000), Accuracy assessments of aerosol optical properties retrieved from AERONET Sun and sky radiance measurements, *J. Geophys. Res.*, *105*, 9791–9806.

Dubovik, O., B. N. Holben, T. F. Eck, A. Smirnov, Y. J. Kaufman, M. D. King, D. Tanre, and I. Slutsker (2002), Variability of absorption and optical properties of key aerosol types observed in worldwide locations, *J. Atmos. Sci.*, *59*, 590–608.

Dutton, E. G., J. J. Michalsky, T. Stoffel, B. W. Forgan, and J. Hickey (2001), Measurement of broadband diffuse solar irradiance using current commercial instrumentation with a correction for thermal offset errors, *J. Atmos. Oceanic Technol.*, *18*, 297–314.

Eck, T. F., B. N. Holben, D. E. Ward, O. Dubovik, J. S. Reid, A. Smirnov, M. M. Mukelabai, N. C. Hsu, N. T. O'Neill, and I. Slutsker (2001), Characterization of the optical properties of biomass burning aerosols in Zambia during the 1997 ZIBBEE field campaign, *J. Geophys. Res.*, *106*, 3425–3448.

Eck, T. F., et al. (2005), Columnar aerosol optical properties at AERONET sites in central eastern Asia and aerosol transport to the tropical mid-Pacific, *J. Geophys. Res.*, *110*, D06202, doi:10.1029/2004JD005274.

Forsythe, J. M., D. L. Randel, S. Woo, D. McKague, and T. H. Vonder Haar (2003), Extending the 12-year NVAP global water vapor dataset into the 21st century, paper presented at 12th Conference on Satellite Meteorology and Oceanography, Am. Meteorol. Soc., Long Beach, Calif., Feb.

Fu, Q., and K. N. Liou (1992), On the correlated k-distribution method for radiative transfer in nonhomogeneous atmospheres, *J. Atmos. Sci.*, *49*, 2139–2156.

Fu, Q., G. Lesins, J. Higgins, T. Charlock, P. Chylek, and J. Michalsky (1998), Broadband water vapor absorption of solar radiation tested using ARM data, *Geophys. Res. Lett.*, *25*(8), 1169–1172.

Geleyn, J. F., and H. J. Preuß (1983), A new data set of satellite-derived surface albedo values for operational use at ECMWF, *Arch. Meteorol. Geophys. Bioklimatol., Ser. A*, *32*, 353–359.

Gilgen, H., and A. Ohmura (1999), The Global Energy Balance Archive, *Bull. Am. Meteorol. Soc.*, *80*, 831–850.

Gilgen, H., M. Wild, and A. Ohmura (1998), Means and trends of shortwave incoming radiation at the surface estimated from Global Energy Balance Archive data, *J. Clim.*, *11*, 2042–2061.

Halthore, R. N., et al. (2005), Intercomparison of shortwave radiative transfer codes and measurements, *J. Geophys. Res.*, *110*, D11206, doi:10.1029/2004JD005293.

Haywood, J. M., and V. Ramaswamy (1998), Global sensitivity studies of the direct radiative forcing due to anthropogenic sulfate and black carbon aerosols, *J. Geophys. Res.*, *103*, 6043–6058.

Hess, M., P. Koepke, and I. Schult (1998), Optical Properties of Aerosols and clouds: The software package OPAC, *Bull. Am. Meteorol. Soc.*, *79*, 831–844.

Holben, B. N., et al. (1998), AERONET-A federated instrument network and data archive for aerosol characterization, *Remote Sens. Environ.*, *66*, 1–16.

Holben, B. N., et al. (2001), An emerging ground-based aerosol climatology: Aerosol optical depth from AERONET, *J. Geophys. Res.*, *106*, 12,067–12,097.

Ichoku, C., D. A. Chu, S. Mattoo, Y. J. Kaufman, L. A. Remer, D. Tanré, I. Slutsker, and B. N. Holben (2002), A spatio-temporal approach for global validation and analysis of MODIS aerosol products, *Geophys. Res. Lett.*, *29*(12), 8006, doi:10.1029/2001GL013206.

Intergovernmental Panel on Climate Change (2001), *Climate Change 2001: The Scientific Basis*, edited by J. T. Houghton et al., 881 pp., Cambridge Univ. Press, New York.

Joseph, J. H., W. J. Wiscombe, and J. A. Weinman (1976), The Delta-Eddington approximation for radiative flux transfer, *J. Atmos. Sci.*, *33*, 2452–2459.

Kahn, R., P. Banerjee, and D. McDonald (2001), The sensitivity of multiangle imaging to natural mixtures of aerosols over ocean, *J. Geophys. Res.*, *106*, 18,219–18,238.

Kahn, R. A., B. J. Gaitley, J. V. Martonchik, D. J. Diner, K. A. Crean, and B. Holben (2005), Multiangle Imaging Spectroradiometer (MISR) global aerosol optical depth validation based on 2 years of coincident Aerosol Robotic Network (AERONET) observations, *J. Geophys. Res.*, *110*, D10S04, doi:10.1029/2004JD004706.

Kato, S., T. P. Ackerman, J. H. Mather, and E. E. Clothiaux (1999), The k-distribution method and correlated-k approximation for a shortwave radiative transfer model, *J. Quant. Spectrosc. Radiat. Transfer*, *62*, 109–121.

Kaufman, Y. J., D. Tanre, L. A. Remer, E. F. Vermote, A. Chu, and B. N. Holben (1997), Operational remote sensing of tropospheric aerosol over land from EOS moderate resolution imaging spectroradiometer, *J. Geophys. Res.*, *102*, 17,051–17,067.

Kaufman, Y. J., I. Koren, L. A. Remer, D. Tanré, P. Ginoux, and S. Fan (2005a), Dust transport and deposition observed from the Terra-Moderate Resolution Imaging Spectroradiometer (MODIS) spacecraft over the Atlantic Ocean, *J. Geophys. Res.*, *110*, D10S12, doi:10.1029/2003JD004436.

Kaufman, Y. J., et al. (2005b), A critical examination of the residual cloud contamination and diurnal sampling effects on MODIS estimates of aerosol over ocean, *IEEE Trans. Geosci. Remote Sens.*, *43*(12), 2886–2897.

Kiehl, J. T., and K. E. Trenberth (1997), Earth's annual global mean energy budget, *Bull. Am. Meteorol. Soc.*, *78*, 197–208.

Kim, D.-H., B. J. Sohn, T. Nakajima, and T. Takamura (2005), Aerosol radiative forcing over east Asia determined from ground-based solar radiation measurements, *J. Geophys. Res.*, *110*, D10S22, doi:10.1029/2004JD004678.

King, M. D., W. P. Menzel, Y. J. Kaufman, D. Tanre, B. C. Gao, S. Platnick, S. A. Ackerman, L. A. Remer, R. Pincus, and P. A. Hubanks (2003), Cloud and aerosol properties, precipitable water, and profiles of temperature and humidity from MODIS, *IEEE Trans. Geosci. Remote Sens.*, *41*, 442–458.

Kinne, S., et al. (2006), An AeroCom initial assessment optical properties in aerosol component modules of global models, *Atmos. Chem. Phys.*, *6*, 1815–1834.

Kneizys, F. X., E. P. Shettle, L. W. Abreu, J. H. Chetwynd, G. P. Anderson, W. O. Gallery, J. E. A. Selby, and S. A. Clough (1988), Users guide to LOWTRAN 7, *Rep. AFGL-TR-88– 0177*, 137 pp., Air Force Geophys. Lab., Bedford, Mass..

Lacis, A. A., and V. Oinas (1991), A description of the correlated k distribution method for modeling nongray gaseous absorption, thermal emission, and multiple scattering in vertically inhomogeneous atmospheres, *J. Geophys. Res.*, *96*, 9027–9063.

Li, Z., and H. G. Leighton (1993), Global climatologies of solar radiation budgets at the surface and in the atmosphere from 5 years of ERBE data, *J. Geophys. Res.*, *98*, 4919–4930.

Li, Z., and A. P. Trishchenko (2001), Quantifying uncertainties in determining SW cloud radiative forcing and cloud absorption due to variability in atmospheric conditions, *J. Atmos. Sci.*, *58*, 376–389.

Li, Z., T. Charlock, and C. Whitlock (1995), Assessment of the global monthly mean surface insolation estimated from satellite measurements using global energy balance archive data, *J. Clim.*, *8*, 315–328.

Li, Z., L. Moreau, and A. Arking (1997), On solar energy disposition: A perspective from observation and modeling, *Bull. Am. Meteorol. Soc.*, *78*, 53–70.

Li, Z., M. Cribb, F. L. Chang, A. Trishchenko, and L. Yi (2005), Natural variability and sampling errors in solar radiation measurements for model validation over the ARM/SGP region, *J. Geophys. Res.*, *110*, D15S19, doi:10.1029/2004JD005028.

Liao, H., and J. H. Seinfeld (1998a), Radiative forcing by mineral dust aerosols: sensitivity to key variables, *J. Geophys. Res.*, *103*, 31,637–31,646.

Liao, H., and J. H. Seinfeld (1998b), Effects of clouds on direct aerosol radiative forcing of climate, *J. Geophys. Res.*, *103*, 3781–3788.

Liepert, B. G. (2002), Observed reductions of surface solar radiation at sites in the United States and worldwide from 1961 to 1990, *Geophys. Res. Lett.*, *29*(10), 1421, doi:10.1029/2002GL014910.

Loeb, N. G., and S. Kato (2002), Top-of-atmosphere direct radiative effect of aerosols over the tropical oceans from the Clouds and the Earth's Radiant Energy System (CERES) satellite instrument, *J. Clim.*, *15*, 1474–1484.

Loeb, N. G., and N. Manalo-Smith (2005), Top-of-atmosphere direct radiative effect of aerosols over global oceans from merged CERES and MODIS observations, *J. Clim.*, *18*, 3506–3526.

Loeb, N. G., N. M. Smith, S. Kato, W. F. Miller, S. K. Gupta, P. Minnis, and B. A. Wielicki (2003a), Angular distribution models for top-of-atmosphere radiative flux estimation from the Clouds and the Earth's Radiant Energy System instrument on the Tropical Rainfall Measuring Mission Satellite. Part I: Methodology, *J. Appl. Meteorol.*, *42*, 240–265.

Loeb, N. G., K. Loukachine, N. M. Smith, B. A. Wielicki, and D. F. Young (2003b), Angular distribution models for top-ofatmosphere radiative flux estimation from the Clouds and the Earth's Radiant Energy System instrument on the Tropical Rainfall Measuring Mission Satellite. Part II: Validation, *J. Appl. Meteorol.*, *42*, 1748–1769.

Loeb, N. G., S. Kato, K. Loukachine, and N. Manalo-Smith (2005), Angular distribution models for top-of-atmosphere radiative flux estimation from the Clouds and the Earth's Radiant Energy System Instrument on the Terra Satellite. Part I: Methodology, *J. Atmos. Oceanic Technol.*, *22*, 338–351.

Long, C. N., and T. P. Ackerman (2000), Identification of clear skies from broadband pyranometer measurements and calculation of downwelling shortwave cloud effects, *J. Geophys. Res.*, *105*, 15,609–15,626.

Lucht, W., C. Schaaf, and A. Strahler (2000), An algorithm for the retrieval of albedo from space using semi-empirical BRDF models, *IEEE Trans. Geosci. Remote Sens.*, *38*, 977–998.
Martonchik, J. V., D. J. Diner, R. Kahn, B. Gaitley, and B. N. Holben (2004), Comparison of MISR and AERONET aerosol optical depths over desert sites, *Geophys. Res. Lett.*, *31*, L16102, doi:10.1029/2004GL019807.
Minnis, P., D. P. Garber, D. F. Young, R. F. Arduini, and Y. Takano (1998), Parameterization of reflectance and effective emittance for satellite remote sensing of cloud properties, *J. Atmos. Sci.*, *55*, 3313–3339.
Myhre, G., A. Grini, J. M. Haywood, F. Stordal, B. Chatenet, D. Tanré, J. K. Sundet, and I. S. A. Isaksen (2003), Modeling the radiative impact of mineral dust during the Saharan Dust Experiment (SHADE) campaign, *J. Geophys. Res.*, *108*(D18), 8579, doi:10.1029/2002JD002566.
Nakajima, T., and M. Tanaka (1986), Matrix formulations for the transfer of solar-radiation in a plane-parallel scattering atmosphere, *J. Quant. Spectrosc. Radiat. Transfer*, *35*, 13–21.
Nakajima, T., and M. Tanaka (1988), Algorithms for radiative intensity calculations in moderately thick atmospheres using a truncation approximation, *J. Quant. Spectrosc. Radiat. Transfer*, *40*, 51–69.
Ohmura, A., and M. Wild (2002), Is the hydrological cycle accelerating?, *Science*, *298*, 1345–1346.
Ohmura, A., et al. (1998), Baseline Surface Radiation Network (BSRN/WCRP): New precision radiometry for climate research, *Bull. Am. Meteorol. Soc.*, *79*, 2115–2136.
Pinker, R. T., B. Zhang, and E. G. Dutton (2005), Do satellites detect trends in surface solar radiation?, *Science*, *308*, 850–854.
Podgorny, I. A., and V. Ramanathan (2001), A modeling study of the direct effect of aerosols over the tropical Indian Ocean, *J. Geophys. Res.*, *106*, 24,097–24,105.
Podgorny, I. A., W. C. Conant, V. Ramanathan, and S. K. Satheesh (2000), Aerosol modulation of atmospheric and solar heating over the tropical Indian Ocean, *Tellus, Ser. B*, *52*, 947–958.
Preuß, H. J., and J. F. Geleyn (1980), Surface albedos derived from satellite data and their impact on forecast models, *Arch. Meteorol. Geophys. Bioklimatol., Ser. A*, *29*, 345–356.
Ramana, M. V., and V. Ramanathan (2006), Abrupt transition from natural to anthropogenic aerosol radiative forcing: Observations at the ABC-Maldives Climate Observatory, *J. Geophys. Res.*, *111*, D20207, doi:10.1029/2006JD007063.
Ramanathan, V., and M. V. Ramana (2005), Persistent, Widespread, and strongly absorbing haze over the Himalayan foothills and the Indo-Ganges plains, *Pure Appl. Geophys.*, *162*, 1609–1626.
Ramanathan, V., and A. M. Vogelmann (1997), Greenhouse effect, atmospheric solar absorption and the Earth's radiation budget: From the Arrhenius/Langley era to the 1990s, *Ambio*, *26*, 38–46.
Ramanathan, V., R. D. Cess, E. F. Harrison, P. Minnis, B. R. Barkstrom, E. Ahmad, and D. Hartmann (1989), Cloud radiative forcing and climate: Results from the Earth Radiation Budget Experiment, *Science*, *243*, 57–63.
Ramanathan, V., et al. (2001a), The Indian Ocean Experiment: An integrated analysis of the climate forcing and effects of the Great Indo-Asian Haze, *J. Geophys. Res.*, *106*, 28,371–28,398.
Ramanathan, V., P. J. Crutzen, J. T. Kiehl, and D. Rosenfeld (2001b), Aerosols, climate, and the hydrological cycle, *Science*, *294*, 2119–2124.
Ramanathan, V., C. Chung, D. Kim, T. Bettge, L. Buja, J. T. Kiehl, W. M. Washington, Q. Fu, D. R. Sikka, and M. Wild (2005), Atmospheric brown clouds: Impacts on South Asian climate and hydrological cycle, *Proc. Natl. Acad. Sci. U. S. A.*, *102*, 5326–5333.
Randel, D. L., T. H. Vonder Haar, M. A. Ringerud, G. L. Stephen, T. J. Greenwald, and C. L. Combs (1996), A new global water vapor dataset, *Bull. Am. Meteorol. Soc.*, *77*, 1233–1246.
Remer, L. A., and Y. J. Kaufman (2006), Aerosol direct radiative effect at the top of the atmosphere over cloud free ocean derived from five years of MODIS data, *Atmos. Chem. Phys.*, *6*, 237–253.
Remer, L. A., et al. (2002), Validation of MODIS aerosol retrieval over ocean, *Geophys. Res. Lett.*, *29*(12), 8008, doi:10.1029/2001GL013204.
Remer, L. A., et al. (2005), The MODIS aerosol algorithm, products and validation, *J. Atmos. Sci.*, *62*, 947–973.
Rieland, M., and E. Raschke (1991), Diurnal variability of the earth radiation budget: Sampling requirements, time integration aspects and error estimates for the Earth Radiation Budget Experiment (ERBE), *Theor. Appl. Climatol.*, *44*, 9–24.
Roderick, M. L., and G. D. Farquhar (2002), The cause of decreased pan evaporation over the past 50 years, *Science*, *298*, 1410–1411.
Roesch, A., C. Schaaf, and F. Gao (2004), Use of Moderate-Resolution Imaging Spectroradiometer bidirectional reflectance distribution function products to enhance simulated surface albedos, *J. Geophys. Res.*, *109*, D12105, doi:10.1029/2004JD004552.
Rossow, W. B., and R. A. Schiffer (1999), Advances in understanding clouds from ISCCP, *Bull. Am. Meteorol. Soc.*, *80*, 2261–2287.
Rothman, L. S., et al. (2003), The HITRAN molecular spectroscopic database: Edition of 20 00 including updates through 2001, *J. Quant. Spectrosc. Radiat. Transfer*, *82*, 5–44.
Rothman, L. S., et al. (2005), The HITRAN 2004 molecular spectroscopic database, *J. Quant. Spectrosc. Radiat. Transfer*, *96*, 139–204.
Russell, P. B., J. M. Livingston, P. Hignett, S. Kinne, J. Wong, A. Chien, R. Bergstrom, O. Durkee, and P. V. Hobbs (1999), Aerosol-induced radiative flux changes off the United States mid-Atlantic coast: Comparison of values calculated from Sun photometer and in situ data with those measured by airborne pyranometer, *J. Geophys. Res.*, *104*, 2289–2307.
Satheesh, S. K., and V. Ramanathan (2000), Large differences in tropical aerosol forcing at the top of the atmosphere and Earth's surface, *Nature*, *405*, 60–63.
Satheesh, S. K., V. Ramanathan, X. Li-Jones, J. M. Lobert, I. A. Podgorny, J. M. Prospero, B. N. Holben, and N. G. Loeb (1999), A model for the natural and anthropogenic aerosols over the tropical Indian Ocean derived from Indian Ocean Experiment data, *J. Geophys. Res.*, *104*, 27,421–27,440.
Schaaf, C., et al. (2002), First operational BRDF, albedo and nadir reflectance products from MODIS, *Remote Sens. Environ.*, *83*, 135–148.
Stanhill, G., and S. Cohen (2001), Global dimming: A review of the evidence for a widespread and significant reduction in global radiation with discussion of its probable causes and possible agricultural consequences, *Agric. For. Meteorol.*, *107*, 255–278.
Stephens, G. L., and S. C. Tsay (1990), On the cloud absorption anomaly, *Q. J. R. Meteorol. Soc.*, *116*, 671–704.
Tanre, D., Y. J. Kaufman, M. Herman, and S. Matto (1997), Remote sensing of aerosol properties over oceans using the MODIS/EOS spectral radiance, *J. Geophys. Res.*, *102*, 16,971–16,988.
Vogelmann, A. M., V. Ramanathan, W. C. Conant, and W. E. Hunter (1998), Observational constraints on non-Lorentzian continuum effects in the near-infrared solar spectrum using ARM ARESE data, *J. Quant. Spectrosc. Radiat. Transfer*, *60*, 231–246.
Vogelmann, A. M., V. Ramanathan, and I. A. Podgorny (2001), Scale dependence of solar heating rates in convective cloud systems with implications to General Circulation Models, *J. Clim.*, *14*, 1738–1752.
Vonder Haar, T. H., J. M. Forsythe, D. L. Randel, and S. Woo (2003), Analysis of the NVAP water vapor dataset: A tool for monitoring Earth's water vapor from daily to decadal scales, paper presented at 12th Conference on Satellite Meteorology and Oceanography, Am. Meteorol. Soc., Long Beach, Calif., Feb.
Wielicki, B. A., B. R. Barkstrom, E. F. Harrison, R. B. Lee III, G. L. Smith, and J. E. Cooper (1996), Clouds and the Earth's Radiant Energy System (CERES): An Earth Observing System experiment, *Bull. Am. Meteorol. Soc.*, *77*, 853–868.
Wielicki, B. A., T. P. Charlock, D. R. Doelling, D. P. Kratz, N. G. Loeb, P. Minnis, K. J. Priestley, and D. F. Young (2006), CERES radiation budget accuracy overview, paper presented at 12th Conference on Atmospheric Radiation, Am. Meteorol. Soc., Madison, Wis., 10–14 July.
Wild, M. (2005), Solar radiation budgets in atmospheric model intercomparisons from a surface perspective, *Geophys. Res. Lett.*, *32*, L07704, doi:10.1029/2005GL022421.
Wild, M., A. Ohmura, and H. Gilgen (1995), Validation of general circulation model radiative fluxes using surface observations, *J. Clim.*, *8*, 1309–1324.
Wild, M., H. Gilgen, A. Roesch, A. Ohmura, C. Long, E. Dutton, B. Forgan, A. Kallis, V. Russak, and A. Tsvetkov (2005), From dimming to brightening: Decadal changes in solar radiation at the Earth's surface, *Science*, *308*, 847–850.
Wild, M., C. N. Long, and A. Ohmura (2006), Evaluation of clear-sky solar fluxes in GCMs participating in AMIP and IPCC-AR4 from a surface perspective, *J. Geophys. Res.*, *111*, D01104, doi:10.1029/2005JD006118.
Young, D. F., P. Minnis, D. R. Doelling, G. G. Gibson, and T. Wong (1998), Temporal interpolation methods for the Clouds and Earth's Radiant Energy System (CERES) experiment, *J. Appl. Meteorol.*, *37*, 572–590.
Yu, H., R. E. Dickinson, M. Chin, Y. J. Kaufman, M. Zhou, L. Zhou, Y. Tian, O. Dubovik, and B. N. Holben (2004), Direct radiative effect of aerosols as determined from a combination of MODIS retrievals and GOCART simulations, *J. Geophys. Res.*, *109*, D03206, doi:10.1029/2003JD003914.
Yu, H., et al. (2006), A Review of measurement-based assessment of aerosol direct radiative effect and forcing, *Atmos. Chem. Phys.*, *6*, 613–666.
Zhang, J., S. A. Christopher, L. A. Remer, and Y. J. Kaufman (2005a), Shortwave aerosol radiative forcing over cloud-free oceans from Terra: 1. Angular models for aerosols, *J. Geophys. Res.*, *110*, D10S23, doi:10.1029/2004JD005008.
Zhang, J., S. A. Christopher, L. A. Remer, and Y. J. Kaufman (2005b), Shortwave aerosol radiative forcing over cloud-free oceans from Terra: 2.

Seasonal and global distributions, *J. Geophys. Res.*, *110*, D10S24, doi:10.1029/2004JD005009.

Zhang, Y. C., W. B. Rossow, A. A. Lacis, V. Oinas, and M. I. Mishchenko (2004), Calculation of radiative fluxes from the surface to top of atmosphere based on ISCCP and other global data sets: Refinements of the radiative transfer model and the input data, *J. Geophys. Res.*, *109*, D19105, doi:10.1029/2003JD004457.

D. Kim, Korea Meteorological Administration, 45 Gisangcheong-gil, Dongjak-gu, Seoul 156-720, South Korea. (dkim@kma.go.kr)

V. Ramanathan, Center for Clouds, Chemistry and Climate, Scripps Institution of Oceanography, 9500 Gilman Drive, #0221, La Jolla, CA 92093, USA.